THE SLOAN DIGITAL SKY SURVEY QUASAR SURVEY: QUASAR LUMINOSITY FUNCTION FROM DATA RELEASE 3

GORDON T. RICHARDS,[1,2] MICHAEL A. STRAUSS,[1] XIAOHUI FAN,[3] PATRICK B. HALL,[4] SEBASTIAN JESTER,[5,6] DONALD P. SCHNEIDER,[7]
DANIEL E. VANDEN BERK,[7] CHRIS STOUGHTON,[5] SCOTT F. ANDERSON,[8] ROBERT J. BRUNNER,[9] JIM GRAY,[10] JAMES E. GUNN,[1]
ŽELJKO IVEZIĆ,[8] MARGARET K. KIRKLAND,[1] G. R. KNAPP,[1] JON LOVEDAY,[11] AVERY MEIKSIN,[12] ADRIAN POPE,[2]
ALEXANDER S. SZALAY,[2] ANIRUDDA R. THAKAR,[2] BRIAN YANNY,[5] DONALD G. YORK,[13,14] J. C. BARENTINE,[15]
HOWARD J. BREWINGTON,[15] J. BRINKMANN,[15] MASATAKA FUKUGITA,[16] MICHAEL HARVANEK,[15]
STEPHEN M. KENT,[5,13] S. J. KLEINMAN,[15] JUREK KRZESIŃSKI,[15,17] DANIEL C. LONG,[15]
ROBERT H. LUPTON,[1] THOMAS NASH,[5] ERIC H. NEILSEN, JR.,[5] ATSUKO NITTA,[15]
DAVID J. SCHLEGEL,[18] AND STEPHANIE A. SNEDDEN[15]

ABSTRACT

We determine the number counts and $z = 0-5$ luminosity function for a well-defined, homogeneous sample of quasars from the Sloan Digital Sky Survey (SDSS). We conservatively define the most uniform statistical sample possible, consisting of 15,343 quasars within an effective area of 1622 deg^2 that was derived from a parent sample of 46,420 spectroscopically confirmed broad-line quasars in the 5282 deg^2 of imaging data from SDSS Data Release 3. The sample extends from $i = 15$ to 19.1 at $z \lesssim 3$ and to $i = 20.2$ for $z \gtrsim 3$. The number counts and luminosity function agree well with the results of the Two Degree Field QSO Redshift Survey (2QZ) at redshifts and luminosities at which the SDSS and 2QZ quasar samples overlap, but the SDSS data probe to much higher redshifts than does the 2QZ sample. The number density of luminous quasars peaks between redshifts 2 and 3, although uncertainties in the selection function in this range do not allow us to determine the peak redshift more precisely. Our best-fit model has a flatter bright-end slope at high redshift than at low redshift. For $z < 2.4$ the data are best fit by a redshift-independent slope of $\beta = -3.1$ [$\Phi(L) \propto L^{\beta}$]. Above $z = 2.4$ the slope flattens with redshift to $\beta \gtrsim -2.37$ at $z = 5$. This slope change, which is significant at the $\gtrsim 5\ \sigma$ level, must be accounted for in models of the evolution of accretion onto supermassive black holes.

Key words: cosmology: observations — galaxies: active — galaxies: luminosity function, mass function — quasars: general — surveys

Online material: machine-readable tables

1. INTRODUCTION

The advent of the Two Degree Field (2dF) QSO Redshift Survey (2QZ; Boyle et al. 2000; Croom et al. 2004) and Sloan Digital Sky Survey (SDSS; York et al. 2000) has resulted in a more than 10-fold increase in the number of known quasars over the past decade. While the evolution of quasars and active galactic nuclei (AGNs) in general has been of considerable interest since the first identification of quasar redshifts (Schmidt 1963, 1968), there has been a resurgence of interest in the subject as a result of recent work in understanding the role of AGNs in galaxy evolution. In particular, the formation of bulges and supermassive black holes at the centers of galaxies appear to be intimately re-lated (the so-called $M_{\rm BH}$-σ relationship; Ferrarese & Merritt 2000; Gebhardt et al. 2000; Tremaine et al. 2002), emphasizing the importance of understanding the role that quasar activity plays in the formation and evolution of the galaxy population as a whole. It has also been argued that feedback mechanisms (e.g., Begelman 2004) may play an important role in determining the $M_{\rm BH}$-σ relationship and the coevolution of black holes and the spheroid component of their host galaxies (e.g., Di Matteo et al. 2003, 2005; Wyithe & Loeb 2003; Granato et al. 2004; Scannapieco & Oh 2004). Furthermore, an accurate description of the quasar luminosity function (QLF) is needed to map the black hole accretion history of the universe (e.g., Yu & Tremaine 2002) and determine how quasars contribute to the feedback cycle.

---

[1] Princeton University Observatory, Peyton Hall, Princeton, NJ 08544.

[2] Department of Physics and Astronomy, The Johns Hopkins University, 3400 North Charles Street, Baltimore, MD 21218-2686.

[3] Steward Observatory, University of Arizona, 933 North Cherry Avenue, Tucson, AZ 85721.

[4] Department of Physics and Astronomy, York University, 4700 Keele Street, Toronto, ON M3J 1P3, Canada.

[5] Fermi National Accelerator Laboratory, P.O. Box 500, Batavia, IL 60510.

[6] School of Physics and Astronomy, Southampton University, Southampton SO17 1BJ, UK.

[7] Department of Astronomy and Astrophysics, Pennsylvania State University, 525 Davey Laboratory, University Park, PA 16802.

[8] Department of Astronomy, University of Washington, Box 351580, Seattle, WA 98195.

[9] Department of Astronomy, University of Illinois at Urbana-Champaign, 1002 West Green Street, Urbana, IL 61801-3080.

[10] Microsoft Research, 301 Howard Street, No. 830, San Francisco, CA 94105.

[11] Astronomy Centre, University of Sussex, Falmer, Brighton BN1 9QJ, UK.

[12] Institute for Astronomy, Royal Observatory, University of Edinburgh, Blackford Hill, Edinburgh EH9 3HJ, UK.

[13] Department of Astronomy and Astrophysics, University of Chicago, 5640 South Ellis Avenue, Chicago, IL 60637.

[14] Enrico Fermi Institute, University of Chicago, 5640 South Ellis Avenue, Chicago, IL 60637.

[15] Apache Point Observatory, P.O. Box 59, Sunspot, NM 88349.

[16] Institute for Cosmic Ray Research, University of Tokyo, 5-1-5 Kashiwa, Kashiwa City, Chiba 277-8582, Japan.

[17] Obserwatorium Astronomiczne na Suhorze, Akademia Pedagogiczna w Krakowie, ulica Podchorążych 2, PL-30-084 Kraków, Poland.

[18] Lawrence Berkeley National Laboratory, 1 Cyclotron Road, MS 50R-5032, Berkeley, CA 94720-8160.

Until recently, the quasar population was parameterized by a broken power law in luminosity with a peak in space density at $z \sim 2-3$. The luminosity at the power-law break has most often been characterized by pure luminosity evolution (PLE), whereby the rarity of luminous quasars today is a result of a fixed population of quasars becoming less luminous with time (Warren et al. 1994; Croom et al. 2004). However, PLE fails beyond the peak (at $z \sim 2.5$) of the luminous quasar space density (Schmidt et al. 1995; Fan et al. 2001). Furthermore, hard X-ray surveys (e.g., Ueda et al. 2003; Barger et al. 2005), which probe both optically obscured AGNs and substantially fainter optical quasars, have found that AGN evolution is best fit by a model in which less luminous AGNs peak in space density at smaller redshifts. This behavior has been termed "cosmic downsizing," whereby the most massive black holes did most of their accreting in the distant past, while less massive objects underwent active accretion in the more recent past (e.g., Cowie et al. 2003; Merloni 2004; Heckman et al. 2004).

While X-ray and infrared surveys (e.g., Ueda et al. 2003; Haas et al. 2004; Treister et al. 2004; Barger et al. 2005; Hasinger et al. 2005) provide a more complete census of nonstellar nuclear activity in galaxies than do optical surveys, and radio surveys have demonstrated that the decline of quasars at high redshift is not due to dust obscuration (Wall et al. 2005), the optical luminosity function remains a powerful diagnostic tool for our understanding of luminous AGNs. This is, in no small part, because of the large areas covered by optical surveys such as the SDSS ($\sim 10,000$ deg^2). Sensitive hard X-ray and infrared surveys, although sampling much higher AGN densities than optical surveys, suffer from much smaller survey areas ($\lesssim 1$ deg^2) and have difficulty constraining the AGN population where it is intrinsically least dense (e.g., the most luminous and highest redshift objects).

This paper presents a long-sought-after result: the optical luminosity function of a large, homogeneous sample of luminous type 1 quasars covering the entire span of observed quasar redshifts. This overall goal has already been roughly met by splicing together different surveys (e.g., Pei 1995): in particular, the combination of results from the 750 deg^2 2QZ survey to $z \sim 2.2$ (Boyle et al. 2000; Croom et al. 2004) (also earlier work, including that of Schmidt & Green [1983], Koo & Kron [1988], Boyle et al. [1988], and Hewett et al. [1993], among others); the photometrically selected COMBO-17 survey (Wolf et al. 2003) spanning $1.2 < z < 4.8$ but only 0.78 deg^2; and $z > 3$ surveys such as Warren et al. (1994), Schmidt et al. (1995), Kennefick et al. (1995), and Fan et al. (2001). Herein we accomplish this goal using a single carefully constructed subset of the SDSS DR3 data that was designed for maximal homogeneity; this subsample has $\sim 15,000$ quasars selected over ~ 1600 deg^2.

This paper describes the luminosity function of quasars with $15.0 < i < 19.1$ and $0.0 \lesssim z \lesssim 3.0$ and extending to $i < 20.2$ for higher redshifts up to $z \sim 5$. The magnitude limits of the SDSS survey only just approach the "break" magnitude ($b_J \sim 19.5$) seen in the 2QZ number counts and are nearly 2 mag brighter than that of the combined SDSS+2dF (2SLAQ) sample from Richards et al. (2005), both of which are restricted to $z \lesssim 2.2$. The SDSS data complement these smaller but deeper optical surveys both by extending to $z \sim 5$ and by having superb multicolor photometry.[19]

In § 2 we describe the creation of a homogeneous statistical sample of quasars from the SDSS data. The selection function is presented in detail in § 3. The less technically minded reader may choose to skip to § 4, where we present the number counts relationship for our sample of quasars. In §§ 5 and 6 we discuss the application of K-corrections to the data and the luminosity function (both binned and maximum likelihood) that we derived after doing so. Finally, some discussion and conclusions are presented in § 7. Throughout this paper we use a Λ cosmology with $\Omega_m = 0.3$, $\Omega_\Lambda = 0.7$, a Hubble constant of $H_0 = 70$ km s^{-1} Mpc^{-1} (e.g., Spergel et al. 2003), and luminosity distances determined according to Hogg (1999) for this cosmology.

2. CONSTRUCTION OF A UNIFORM QUASAR SAMPLE

2.1. The Parent Sample

The SDSS is an imaging and spectroscopic survey of the high Galactic latitude sky in the Northern Hemisphere (York et al. 2000). It uses a dedicated wide-field 2.5 m telescope (Gunn et al. 2006) at Apache Point Observatory, New Mexico, with a 140 megapixel imaging camera (Gunn et al. 1998) and a pair of fiber-fed multiobject double spectrographs. The imaging is carried out in five broad bands (*ugriz*; Fukugita et al. 1996, Stoughton et al. 2002) on photometric moonless nights of good seeing (Hogg et al. 2001). The imaging data are processed with a series of pipelines (Lupton et al. 2001; Pier et al. 2003), resulting in astrometric calibration errors of $<0\farcs1$ rms per coordinate, and photometric calibration to better than 0.03 mag (Smith et al. 2002; Ivezić et al. 2004; Tucker et al. 2005). The photometry we use is corrected for Galactic extinction using the maps of Schlegel et al. (1998). Spectroscopic targets, including quasar candidates (Richards et al. 2002), are selected from the imaging catalogs and assigned to spectroscopic tiles (Blanton et al. 2003a), and spectra are obtained. These data have been made publicly available in a series of data releases (EDR: Stoughton et al. 2002; DR1: Abazajian et al. 2003; DR2: Abazajian et al. 2004; DR3: Abazajian et al. 2005; DR4: Adelman-McCarthy et al. 2006).

Main survey quasar candidates are selected for spectroscopic follow-up as described in Richards et al. (2002). The quasar candidates are distinguished from the much more numerous stars and normal galaxies in the SDSS in two ways: either by having distinctive *ugriz* colors (subdivided into *ugri* [$z \lesssim 3.0$, where most sources are UV-excess] and *griz* [$z \gtrsim 3.0$] selection criteria) *or* by having FIRST (Becker et al. 1995) 20 cm radio counterparts. Quasars with redshifts around 2.7 and 3.5 have colors very close to those of normal stars (Fan 1999), which greatly decreases the efficiency and completeness of the quasar sample in the vicinity of these redshifts. Radio selection, while adding less than 1% to the color-selected sample (as most radio-selected quasars are also color-selected; Ivezić et al. 2002), helps to improve our selection completeness at these redshifts. Accounting for this and other sources of incompleteness is the focus of § 3.

The spectroscopically confirmed quasars (restricted to those objects that meet a traditional quasar definition [$M_i < -22$ measured in the rest frame and a full width at half-maximum of lines from the broad-line region greater than 1000 km s^{-1}]) in the SDSS have been published by Schneider et al. (2005, hereafter DR3Q), and the current study uses this quasar sample as its basis. The quasar identifications and redshifts in DR3Q are identical to those in the DR3 online database itself in most cases, but visual inspection has caused the redshifts and line widths of several hundred objects to be corrected.

2.2. Statistical Sample Construction

The DR3Q sample contains 46,420 quasars, but as the QLF requires the most homogeneous data set possible, we wish to use

---

[19] Work on the QLF at $z \sim 6$ involves going beyond the main selection algorithm of SDSS (Fan et al. 2001).

only the subset of objects that were selected uniformly with the quasar target selection algorithm described by Richards et al. (2002). In particular, we reject several classes of object:

1. Objects selected for spectroscopy by algorithms other than the main quasar target selection code (especially various "serendipity" algorithms; Stoughton et al. 2002; Anderson et al. 2003) are rejected. Most of these additional quasars are fainter than the $i = 19.1$ mag limit of the UV-excess branch of quasar target selection. This rejects close to 28% of the quasars in the DR3Q sample.

2. The original version of the quasar target selection algorithm used in the EDR and DR1 (including data taken through 2001 June) did a particularly poor job of selecting quasars with redshifts close to $z = 3.5$. Explicit color cuts, implemented for targets new to DR2 and beyond, much improved the situation. In this paper we restrict ourselves solely to quasars selected using this improved algorithm (ver. v3_1_0 of the target selection algorithm), as described by Richards et al. (2002), thus rejecting nearly half of the DR3Q quasars. Figure 1 compares the redshift distribution for quasars from before and after the changes in the algorithm; the $z > 3$ region is much better (but still not perfectly) sampled with the final algorithm. The Appendix shows the Structured Query Language (SQL) query that we used to select the resulting subsample from the SDSS Catalog Archive Server (CAS). This query resulted in 53,459 quasar candidates selected over 2520 deg² of sky,[20] of which 18,966 are matched to spectroscopically confirmed quasars from the DR3Q.[21]

3. The quasar target selection algorithm searches for outliers from the stellar locus in color space and, as such, is very sensitive to data with large photometric errors due to problems in photometric calibration or in point-spread function (PSF) determination. As we describe in § 2.3, we identify problematic stellar loci on a field-by-field basis (a field is an SDSS image in all five bands, with approximate dimensions of $13' \times 10'$) and reject quasar candidates selected from these fields. Roughly 21% of all DR3 quasar candidates are rejected in this stage.

Because of the evolution of the image-processing software (Lupton et al. 2002; Abazajian et al. 2003), the SDSS includes two versions of PSF photometry for each object: the TARGET photometry (using the version of the pipeline and calibration current at the time quasar target selection was carried out) and the BEST photometry (using the most recent version of the pipeline at the time of the data release). The differences between the two are subtle, but only 94% of the DR3Q quasars in the computer sample were selected from both TARGET and BEST photometry (most of the discrepant objects are near the magnitude or color boundaries of the selection criteria). The spectroscopic sample is (close to) complete only in TARGET, which is what we use here to construct a homogeneous statistical sample.

2.3. Image Quality Restrictions

Because of the sensitivity of the quasar target selection algorithm to data of poor photometric quality, we identify and reject such data from further consideration in this analysis.

As described by Ivezić et al. (2004) and Abazajian et al. (2005), the quality of the PSF can be tested by examining the difference between PSF and large-aperture photometry of bright stars on a field-by-field basis. Thus, any field in which the me-
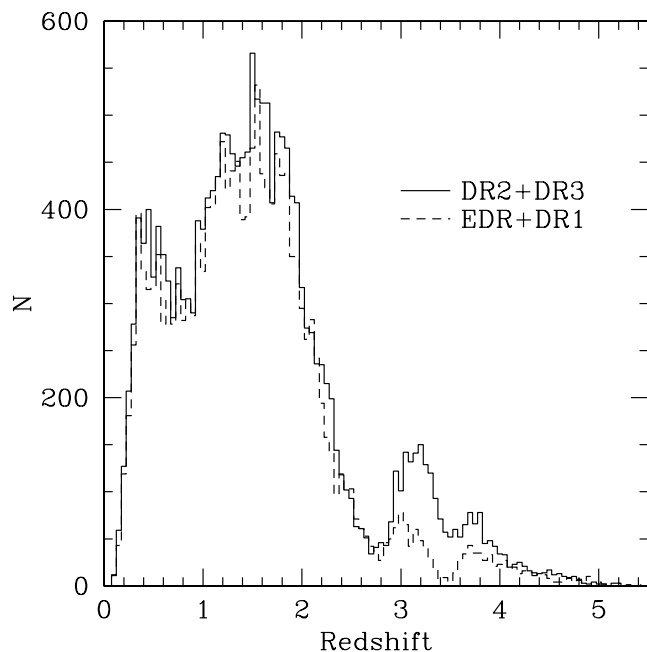
Fig. 1.—Comparison of the SDSS quasar redshift distribution before (EDR+DR1; *dashed line*) and after (DR2+DR3; *solid line*) the Richards et al. (2002) selection algorithm was put in place; the two subsamples have similar numbers of objects. Note the improvement in completeness at $z = 3-4$ for the objects discovered after DR1. At lower redshift ($z \lesssim 2$), quasars are selected largely by UV excess, and the EDR and DR1 samples show no evidence of incompleteness. The structure in the redshift distribution is due to selection effects (see § 3).

dian difference between these quantities was more than a 3 σ outlier (with respect to the entire DR3 sample) in any of the five bands was rejected.

As a further check on the quality of the data, we take advantage of the fact that the locus of stars in color-color space (e.g., Finlator et al. 2000) is remarkably narrow (0.03 mag or less in most projections) and uniform over the sky. The ridge lines of the stellar locus allow one to define a series of "principal colors" (Ivezić et al. 2004); deviations of the principal colors from their canonical values or increases in the width of the stellar locus are indications of inferior data. The median principal color in a running four-field boxcar and the rms principal color around the median are available in the SDSS *runQA* outputs for each field. We rejected fields in which any of the four principal colors deviated from the mean (for that run) by more than 3 σ.

However, the statistics of the rms widths of the principal color distributions per field show considerable variation from run to run, with some runs showing substantially narrower principal color distributions than others. Thus, if a given field had an rms width 5 σ greater than the mean width overall of DR3, that field was rejected. On the other hand, if the rms widths for a field were 3 σ greater than the mean for the given run but less than 2 σ relative to all of DR3, the field was retained.

Finally, we required that the r-band seeing be less than $2''.0$ and that the operational database quality flag for that field not be BAD, MISSING, or HOLE (these typically flag missing fields or fields in which the photometric pipeline was unable to process the data; see the discussion in § 4.6 of Stoughton et al. [2002]).

These restrictions reject 16.9% of the area considered in our initial query and remove 11,186 of the 53,459 quasar candidates (20.9%), leaving a cleaned statistical sample of 15,343 quasars (down from 18,966). The removed fields have a higher-than-average density of quasar candidates, a reflection of the fact that inferior photometry tends to push stars out of the stellar locus.
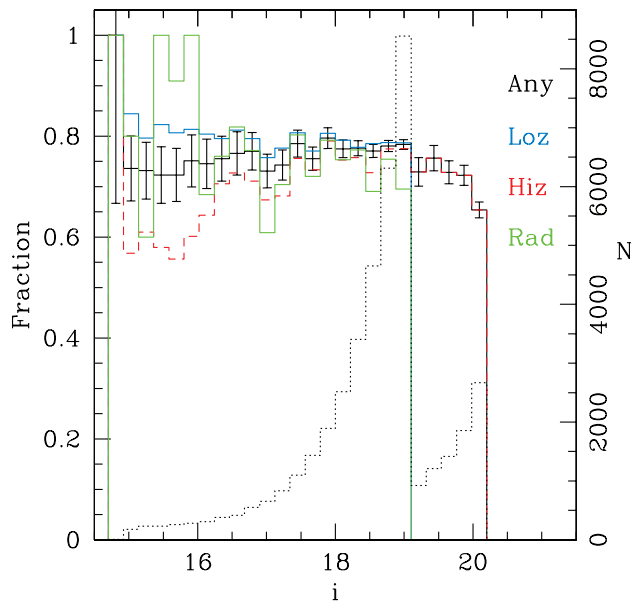
FIG. 2.—Fraction of quasar targets (from TARGET photometry) with spectroscopic observations. Different classes of quasars are marked separately: *black*, all (with Poisson error bars superposed); *blue*, *ugri* ($z \lesssim 3$)–selected (Loz); *red*, *griz* ($z \gtrsim 3$)–selected (Hiz); *green*, radio-selected (Rad). The average completeness for all $i \leq 19.1$ targets is 77.44%. Almost all the incompleteness is due to the lag of the SDSS spectroscopic survey with respect to the imaging survey. The right axis and the dotted line show the number of DR3Q quasars as a function of magnitude.

FIG. 3.— Quasar selection efficiency as a function of magnitude in our statistical sample of SDSS quasar candidates. The overall efficiency is given by the solid line, with Poisson error bars superposed. The dashed line shows the low-z selection (*ugri*) only, excluding quasars fainter than $i = 19.1$. The dotted line shows the efficiency for UV-excess quasar candidates with $u - g < 0.6$ and $g - i > -0.3$ and $i \leq 19.1$. Note that fainter than $i = 19.1$ the efficiency of the *griz* branch of the code is substantially smaller. The overall efficiency of the algorithm for all quasar candidates, *ugri*-selected quasars, and UV-excess-selected quasars is 49%, 61%, and 77%, respectively.

2.4. *Effective Area and Quasar Selection Efficiency*

Calculating the luminosity function requires determining the solid angle of the survey. Of the 5282 deg^2 of the DR3 imaging, 2520 deg^2 was targeted using version v3_1_0 (or later) of the target selection algorithm and is thus covered by the query in the Appendix. Of this area, 426 deg^2 are rejected as having inferior photometry, as described in § 2.3, leaving 2094 deg^2. Only 0.05% of the sky is unsearchable for quasars due to nearby bright stars (Scranton et al. 2002), which is smaller than our uncertainty in the total area (see below); thus, we have not taken this correction into account.

For technical reasons, it is cumbersome to combine the geometric information on the imaging and spectroscopic sky coverage, so we use an empirical technique to determine the fraction of these 2094 deg^2 for which we have spectroscopy. We simply determine the completeness of the quasar candidate spectroscopy (Fig. 2) and multiply the total area by this fraction to find the effective area. The spectroscopic completeness (fraction of quasar targets with spectra) for targets with $i < 19.1$ is 77.4% (fainter than 19.1, we are increasingly sensitive to regions of poor photometry). The tiling algorithm is more than 99% complete (Blanton et al. 2003a), so this 22.6% incompleteness reflects the area of sky not yet covered by spectroscopy. Thus, the effective area covered by our sample is 1622 deg^2. The uncertainty on this area is of order 10 deg^2, most of which comes from the empirical correction to the difference between the imaging and spectroscopic area.

Richards et al. (2002) describe the efficiency (fraction of quasar candidates that are indeed quasars) of the quasar target selection algorithm; we revisit this with the clean data we have described here. Figure 3 shows the fraction of spectroscopically confirmed quasars among the quasar targets with spectroscopy as a function of magnitude. The efficiency is worse at brighter magnitudes, as the ratio of stars to quasars increases dramatically at the bright
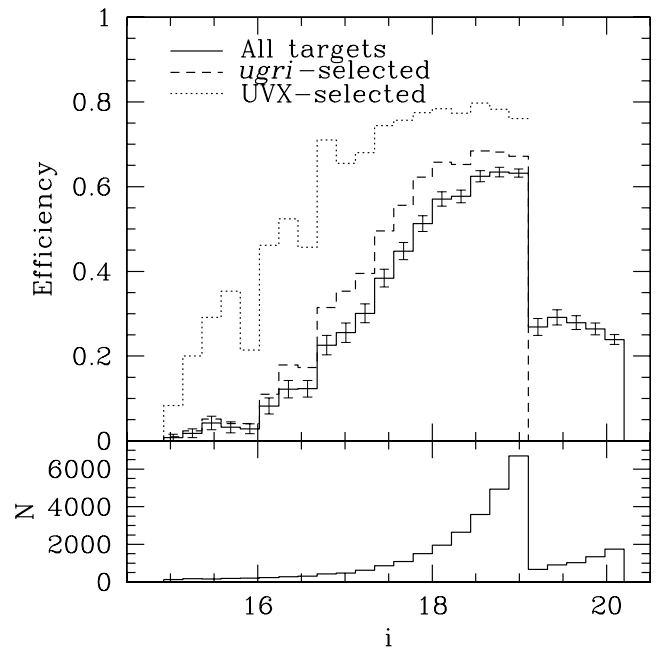
end. The dashed line gives the efficiency of our *ugri* ($z \lesssim 3$) selection, which is appreciably higher than that for all objects. Fainter than $i = 19.1$, candidates are from the *griz* selection, where the efficiency is known to be significantly lower than that for the $i < 19.1$ selection. The dotted line shows the efficiency of a simple selection for UV-excess sources (defined here as sources with $u - g < 0.6$ and $g - i > -0.3$, the latter cut removing most hot white dwarfs); this efficiency is close to 80%. The principal contaminant of the UV-excess sources is emission-line galaxies. The overall efficiencies of the algorithm for all quasar candidates, *ugri*-selected quasars, and UV-excess-selected quasars are 49%, 61%, and 77%, respectively. Correcting for any remaining bad fields (§ 2.3) and counting lower luminosity AGNs (i.e., Seyfert [1943] galaxies), narrow-line AGNs (e.g., Heckman 1980; Zakamska et al. 2003), and BL Lac objects (e.g., Collinge et al. 2005) would further increase the selection efficiency of AGNs in general (cf. the 66% overall efficiency given in Richards et al. [2002]).

3. SELECTION FUNCTION AND THE COMPLETENESS OF THE QUASAR SAMPLE

The quasar target selection algorithm is a function of observed colors, magnitudes, and radio brightness and is sensitive to the completeness and photometric errors of the SDSS imaging data. In this section we determine the selection function of the sample, i.e., the completeness as a function of apparent magnitude and redshift.

3.1. *Image Quality Completeness*

We start with the incompleteness due to the SDSS imaging data and photometric pipeline. In particular, as described by Richards et al. (2002), objects with the so-called fatal and nonfatal flags from the photometric pipeline, indicating unreliable photometry of the object, are precluded from being selected on
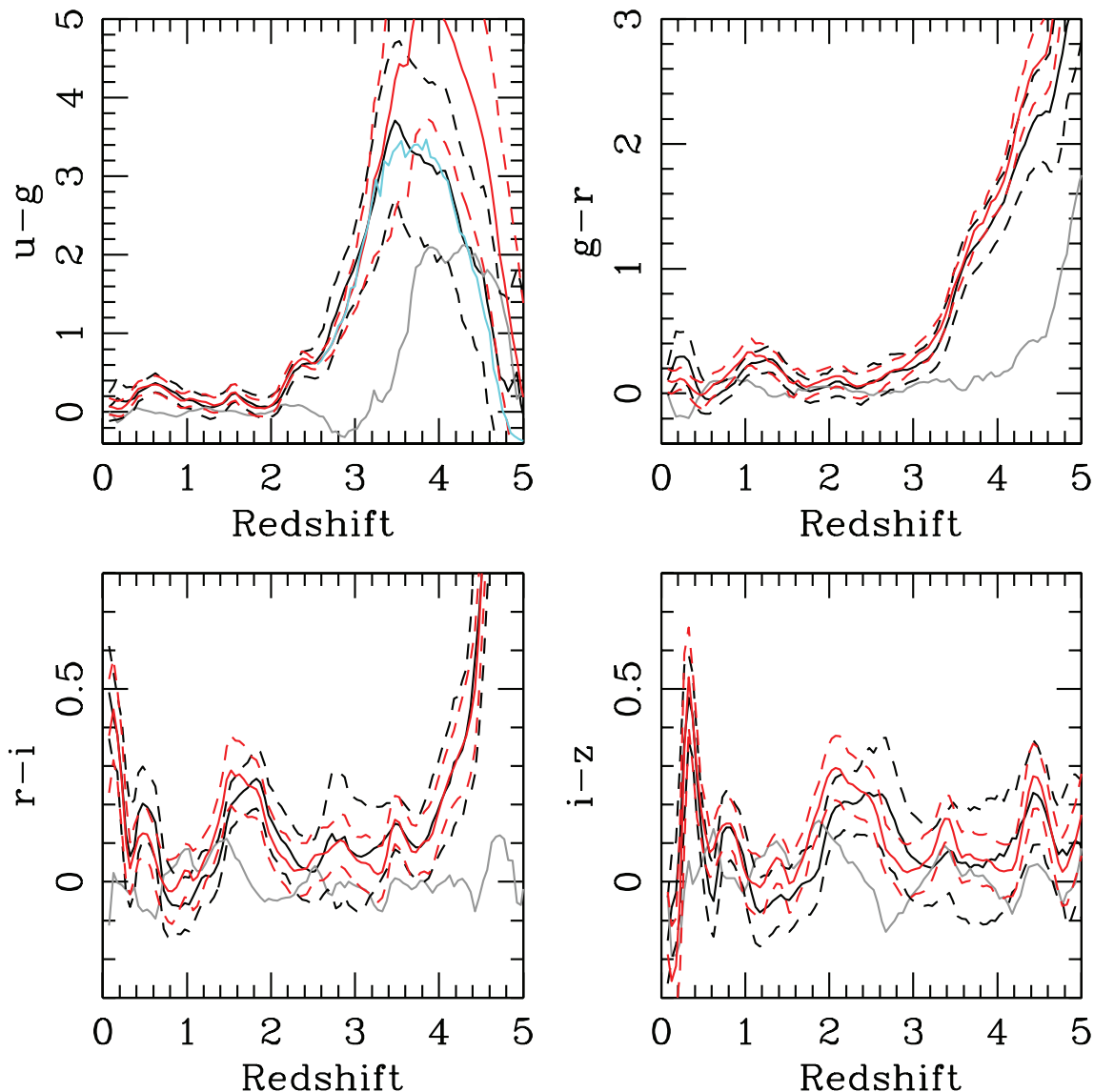
FIG. 4.—Mean DR3Q quasar colors (*solid black lines*) and 68% confidence limits (*dashed black lines*) and mean simulated quasar colors (*solid red lines*) and 68% confidence limits (*dashed red lines*), all as a function of redshift. Gray lines show the difference between the simulated and observed means. The cyan line at high redshift in the top left panel represents the mean magnitude-weighted simulated quasar color; this weighting properly accounts for the effect of asinh magnitudes at low signal-to-noise ratio and is a much better match to the data.

the basis of their colors. Vanden Berk et al. (2005) have determined that 3.8% of all point sources brighter than $i = 19.1$ are excluded because of these flags; this fraction is a (weak) function of magnitude.[22]

In the magnitude range $17.5 < i < 18.5$, roughly 94% of 2QZ (Croom et al. 2004) quasars, based on completely independent imaging data, are recovered by SDSS, suggesting an SDSS image quality completeness of this order, in good agreement with what we found above. Similarly, at the bright end, 17 out of 18 (94%) $z > 0.3$ Palomar-Green (PG; Schmidt & Green 1983) quasars in the DR3 sample footprint are free of cosmetic defects in the SDSS imaging (see the discussion in Jester et al. 2005). We thus apply a global 5% correction (splitting the difference between the 94% image quality completeness from these compar-

isons and the 96% value from Vanden Berk et al. [2005]) to account for image quality incompleteness.

3.2. Simulated Quasars

Fan (1999) describes the construction of simulated quasar photometry in the SDSS photometric system. These simulations are run through the quasar target selection code, allowing us to quantify the fraction of objects selected as a function of magnitude and redshift. The simulations used herein are similar to those of Fan (1999; see also Fan et al. [2001] and Richards et al. [2003]), modulo some changes in the relative strengths of the emission lines, adoption of a redder continuum shortward of Lyα emission, and the use of a more recent characterization of the SDSS filter curves (Stoughton et al. 2002).

The colors of each simulated quasar are determined by the power-law index α_ν of its continuum ($f_\nu \propto \nu^{\alpha_\nu}$), the strength of its emission lines, the absorption of the Lyα forest and presence of Lyman limit systems, and its redshift. For the power-law

---

[22] This magnitude dependence, however, may be due to the fact that the Vanden Berk et al. (2005) sample is mostly stars, which have a different color and Galactic latitude dependence than do quasars.
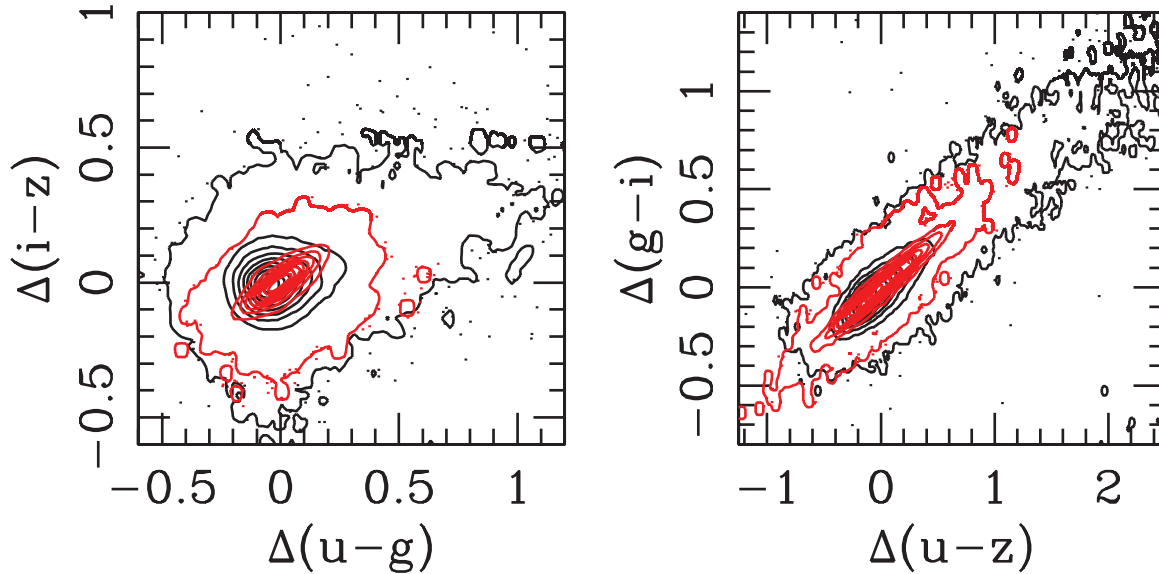
Fig. 5.—Relative colors of DR3 quasars (*black contours and dots*) and simulated quasars (*red contours and dots*). Only quasars with $0.6 < z < 2.2$ and $i < 19.1$ are considered. Overall, the simulations match the data quite well, but the data clearly show red outliers and objects with convex SEDs that are not described by the simulations. Objects with pure power-law continua and no photometric errors would show perfect correlation between the relative colors.

continuum, the simulations assume a Gaussian distribution in α_ν, with a mean of -0.5 and standard deviation of 0.3. This mean spectral index is in reasonable agreement with the composite SDSS quasar spectrum given by Vanden Berk et al. (2001), who find $\alpha_\nu = -0.46$. At wavelengths shortward of the Lyα emission line we instead use a spectral index derived from a Gaussian distribution with a mean of -1.57 and dispersion of 0.17, consistent with the results of Telfer et al. (2002);[23] this spectral index is taken to be uncorrelated with that used at longer wavelengths. Note that the use of this steeper spectral index shortward of Lyα represents a significant change from our previous use of these simulations (such as discussed in Richards et al. 2002), in which we generally used the same power law for all optical/UV wavelengths; we discuss below how this affects the $z > 2.2$ selection function.

We simulate 200 quasars at each grid point in apparent magnitude and redshift space, with an additional 1000 quasars on grid points with $1.8 < z < 3.2$, where the selection efficiency is low. The magnitude grid points are separated by 0.1 mag in the range $13 < \mathrm{AB}_{1\,\mu m} < 22.4$ in asinh magnitudes (Lupton et al. 1999; Stoughton et al. 2002), fully spanning the space of the SDSS imaging data.[24] The redshift grid points span the range $0 < z < 5$, spaced at intervals of 0.05. We add errors to the magnitudes consistent with the estimated PSF magnitude errors in the SDSS photometric pipeline (see Fan 1999); they are Poisson-distributed in flux space so that we properly reproduce the rollover of the asinh magnitude errors (Lupton et al. 1999). Errors from photometric calibration uncertainties (e.g., Ivezić et al. 2004; Tucker et al. 2005) of 0.02 mag are added in quadrature to the g, r, and i measurement and 0.03 mag to the u and z measurement. The output

of the simulations is the *ugriz* photometry and errors of each object, which can be input directly into the target selection code. Any object with errors of greater than 0.2 mag (i.e., less than a 5 σ detection) in a given band is considered to be undetected in that band.

Figure 4 compares the observed (*black lines*) and simulated (*red lines*) SDSS colors of quasars as a function of redshift; both the mean colors and the contours containing 68% of the quasars at each redshift are shown. The difference between the observed and simulated mean colors as a function of redshift is given by the gray lines. In general, the simulated colors trace the observed colors quite well. At higher redshifts, where Lyα forest absorption causes asinh and logarithmic magnitudes to exhibit magnitude-dependent differences, it is important to determine a properly magnitude-weighted mean for the simulations for comparison with the data, as shown by the cyan line in Figure 4 (*top left*).

We next compare the *range* of colors between simulations and observations. Following Richards et al. (2001, 2003) we subtract the mean color as a function of redshift from the observed color, removing the mean emission-line contribution from the colors and allowing for a redshift-independent color comparison. This process allows for more robust comparison of quasar colors across a wide range of redshifts (as compared to using disparate continuum windows at low and high redshift). These relative colors [$\Delta(u - g)$, etc.] of quasars with $0.6 < z < 2.2$ and $i < 19.1$ are plotted against each other for both the data and simulations in Figure 5. The simulations reproduce the overall trends in relative color; the differences reflect the sense in which the optical/UV continua of quasars are not perfectly described by power laws. The simulations and data agree well in the $\Delta(u - z)$, $\Delta(g - i)$ plane, but $\Delta(u - g)$ and $\Delta(i - z)$ are much less correlated in the data than in the simulations. Power laws produce an exact correlation between these relative colors in the absence of errors. We find that the $\Delta(u - g)$ color is within 3 σ of the $\Delta(i - z)$ color for 78% of the observed quasars, while this fraction is 94% for the simulated quasars. Thus, roughly 16% of the quasars in our sample have continua that deviate significantly from a power law.

Dust reddening (e.g., Richards et al. 2003; Hopkins et al. 2004) can explain at least some of the (comparatively) red tail of

---

[23] A much harder (i.e., bluer) UV color was derived from a less luminous, low-redshift sample of quasars studied by the *Far Ultraviolet Spectroscopic Explorer* (Scott et al. 2004). We found that using this bluer continuum did a poorer job of matching the observed redshift histogram; see Fig. 9.

[24] The simulations are normalized at 1 μm, a local minimum in the spectral energy distribution (SED) of quasars (Elvis et al. 1994), as working longward of the effective wavelength of the SDSS i band allows us to match the bluer observed color distribution of the brightest quasars (e.g., Jester et al. 2005).
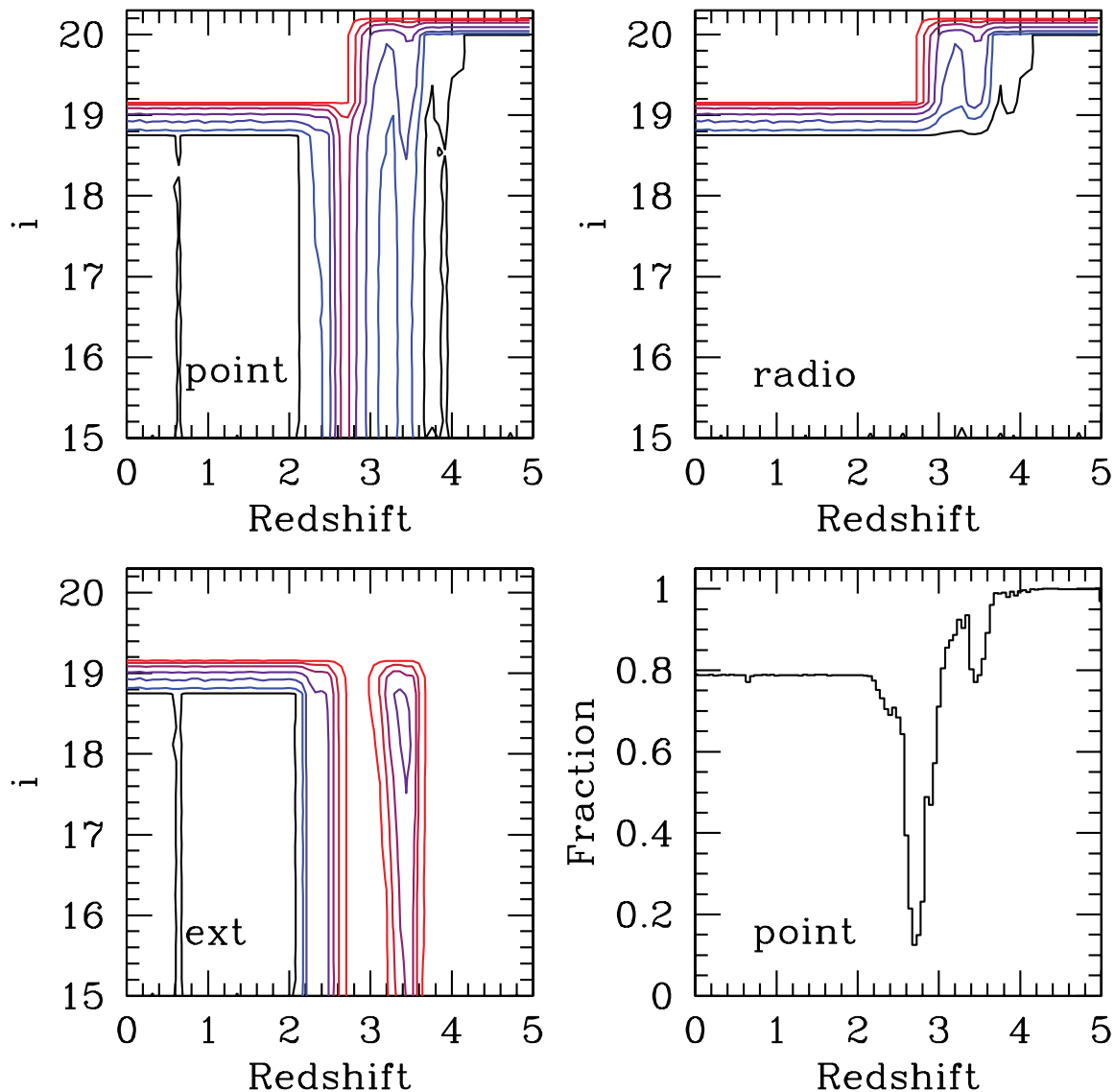
Fig. 6.—Quasar target selection completeness from the simulations as a function of redshift and *i* magnitude for nonradio point (*point*), radio point (*radio*), and extended (*ext*) sources. Contours are at 1%, 10%, 25%, 50%, 75%, 90%, and 99% completeness. The 99% completeness limit is shown in black; the 1% limit is shown in red. The bottom right panel shows the completeness of nonradio point sources from the top left panel, averaged over $15 < i < 20.2$. Recall that the limiting magnitude changes from $i = 19.1$ to $i = 20.2$ at $z \approx 3$.

the relative color distribution and those objects with red (more positive) $\Delta(u - g)$ and blue (more negative) $\Delta(i - z)$, as the simulations do not include the effects of dust. However, the fraction of such reddened objects is relatively small. Richards et al. (2003) estimate that 6% of broad-line (type 1) quasars in the SDSS are consistent with being moderately reddened by dust. Objects with blue $\Delta(u - g)$, red $\Delta(i - z)$ objects must instead be due to either photometric errors, atypical emission-line ratios, or intrinsic (convex) curvature. The latter objects may be interesting for comparison with accretion disk model spectral energy distributions (SEDs) (e.g., Hubeny et al. 2000).

3.3. *Completeness of the Quasar Sample*

We apply the quasar target selection algorithm, using the version described by Richards et al. (2002), to the simulated quasar colors. As we have discussed, the target selection algorithm includes both color and radio selection. For all practical purposes the selection algorithm considers objects as fitting into one of

three classes: point sources without radio detections, point sources with radio detections, and extended sources. To simulate radio sources we simply set the flag that says that the object is detected in the radio. For extended sources we similarly set the extended flag (but note that the simulations do not include any host galaxy contribution to the magnitudes or colors).

Figure 6 shows the completeness of the algorithm as a function of redshift and *i* magnitude for radio sources, nonradio point sources, and extended sources. Contours are at 1%, 10%, 25%, 50%, 75%, 90%, and 99% completeness. The 99% completeness limit is shown by the black line, and 1% is shown by the red line. This figure and the two following are similar to those shown in Richards et al. (2002) but use the updated quasar simulations as discussed above. The selection function shown in Figure 6 is also given in Table 1. The columns give the *i*-band magnitude, the redshift, and the selection function for nonradio point sources, radio-detected point sources, and extended sources; image quality completeness is not included.

i mag	z_{em}	Point	Radio	Extended
15.0.............................	0.00	1.000	1.000	1.000
15.0.............................	0.05	1.000	1.000	1.000
15.0.............................	0.10	1.000	1.000	1.000
15.0.............................	0.15	1.000	1.000	1.000
15.0.............................	0.20	1.000	1.000	1.000
15.0.............................	0.25	1.000	1.000	1.000
15.0.............................	0.30	1.000	1.000	1.000
15.0.............................	0.35	1.000	1.000	1.000
15.0.............................	0.40	1.000	1.000	1.000
15.0.............................	0.45	1.000	1.000	1.000
15.0.............................	0.50	1.000	1.000	1.000
15.0.............................	0.55	1.000	1.000	1.000
15.0.............................	0.60	1.000	1.000	1.000
15.0.............................	0.65	0.980	1.000	0.975
15.0.............................	0.70	0.995	1.000	0.990
15.0.............................	0.75	1.000	1.000	1.000
15.0.............................	0.80	1.000	1.000	1.000
15.0.............................	0.85	1.000	1.000	1.000
15.0.............................	0.90	1.000	1.000	1.000
15.0.............................	0.95	1.000	1.000	1.000

NOTE.—Table 1 is published in its entirety in the electronic edition of the *Astronomical Journal*. A portion is shown here for guidance regarding its form and content.

Table 1 and the selection function plots give the fraction of true quasars at a given redshift and apparent magnitude that would be selected. Brighter than the magnitude limit, the selection function is only weakly dependent on magnitude, and we show the marginalized selection function in Figure 6 (*bottom right*). Thus, each object is assigned a weight (inverse of the value of the selection function) depending on its redshift and apparent magnitude in the determination of the luminosity function below. Not surprisingly, the selection function is particularly low at redshift 2.7, where quasars have colors very similar to A–F stars. There is a secondary dip at $z \approx 3.5$, where quasars have similar colors to G–K stars in the *griz* diagram.

The selection function for extended sources beyond $z = 2.2$ is very low, as expected. Radio source selection does not depend on color; thus, the radio selection function shows no dependence on redshift except at redshifts above 3 and $i > 19.1$, where the only radio-detected objects are those selected by the *griz* algorithm.

Figure 7 (*left panels*) shows the completeness as a function of redshift and absolute i magnitude. These panels are a simple transformation of variable from Figure 6 (*left panels*), but this presentation is helpful for comparison with the luminosity function (§ 6). Selection of radio sources is independent of color; thus, we exclude this panel in Figure 7. Figure 7 (*right panels*) shows our completeness as a function of redshift and optical spectral index (α_ν). In the $2.2 < z < 3$ regime, intrinsically bluer sources are much more likely to be selected than red sources, and the redshift dependence of the selection function is seen to be color-dependent.

Figure 8 overplots the redshift distribution of the quasar sample and the value of the selection function for each quasar (including radio sources). The division between the low-redshift and high-redshift branches of the target selection algorithm, with their different magnitude limits, is at $z \sim 3$. The fainter magnitude limit for $z \geq 3$ greatly exaggerates the discontinuity already present because of the rapidly changing selection function at this redshift. The excess of quasars at $z \sim 0.4$ is likely due to uncorrected host galaxy (and emission line; see § 5) flux, which

makes these quasars appear brighter than they should (and thus selected to a fainter intrinsic magnitude limit).

In the vicinity of $z \sim 2.7$, the selection function drops precipitously and is quite sensitive to such uncertain details of the simulation as the mean and distribution function of the slope of the UV continuum. Indeed, Figure 5 shows that the simulations do not perfectly model the observed quasar color distribution; these details mean that the large value of the correction at this redshift is quite uncertain. We therefore somewhat arbitrarily place a lower limit of 0.333 on the selection function to avoid overcorrecting for incompleteness at these redshifts. This choice is based on our expectations regarding smoothness of the quasar distribution with redshift in the absence of selection effects (e.g., see § 3.4). Imposing this lower limit affects 285 quasars with $z \sim 2.7$, or 2% of the full sample (22% of quasars with $2.2 \leq z \leq 3.0$). The need for imposing this limit may be indicative of quasars having somewhat bluer colors than the mean that we assume for the simulations, bluer quasars being more likely to be selected than redder quasars at $z \sim 2.7$; see Figure 7 (*top right*).

The changing magnitude limit near $z \sim 3$ and the effects of emission lines (see § 5) make it impossible to simply correct the raw redshift histogram in Figure 8. However, after correcting for the selection effects discussed above, removing extended sources, and limiting the sample to $i = 19.1$ *after* applying the emission-line K-correction discussed in § 5, we find a rather smooth redshift distribution, which is shown by the gray line in Figure 8.

More appropriate to the determination of the QLF is to examine the redshift distribution of an absolute magnitude portion of the sample. We see below that quasars with $M_i < -27.6$ (after applying a nonstandard K-correction; see § 5) fall within our magnitude limits for $0.8 < z < 4.8$. Thus, Figure 9 shows the raw (*dashed line*) and corrected (*solid line*) distribution of $M_i < -27.6$ quasars. The corrected histograms include the floor on the selection function of 0.333, which is applied throughout the rest of this work. The error bars in Figure 9 are derived from summing the squared weights for each object (*without* the floor in the selection function) in each bin; note the particularly large errors at $z \approx 2.7$.

While the resulting redshift histogram is indeed quite smooth, we have found that the results are quite sensitive to the details of the simulations, given the sharp gradients of the selection function with redshift. Small changes in the assumed UV spectral index distribution in the simulated quasar spectra change the exact redshift of the minimum of the selection function, producing dramatic changes in the corrected redshift histogram. Thus, Figure 9 also gives the corrected distribution for two other simulations to give the reader an idea of the possible range of corrections. Figure 9 (*dotted line*) shows a correction for a simulation that also has a UV slope of approximately -1.5 (similar to Telfer et al. 2002) but with the O VI equivalent width increased by 20 Å. This simulation produces a very strong, narrow peak near $z \sim 2.5$ but leaves a deficit near $z \sim 2.8$. Similarly, the dot-dashed line uses parameters identical to those of our principal simulation but has a UV spectral index of -0.5, following Scott et al. (2004). This simulation produces a narrow peak near $z \sim 3.0$ but leaves a hole at $z \sim 2.6$. We see in § 3.4 that the set of simulations that we have chosen (as illustrated by the solid line in Fig. 9) is supported a posteriori by a comparison between the radio and color selection.

3.4. Radio Selection versus Color Selection

Quasars selected because of their radio properties provide an independent probe of our quasar selection function. These sources are selected independent of their optical colors; thus, 100% of
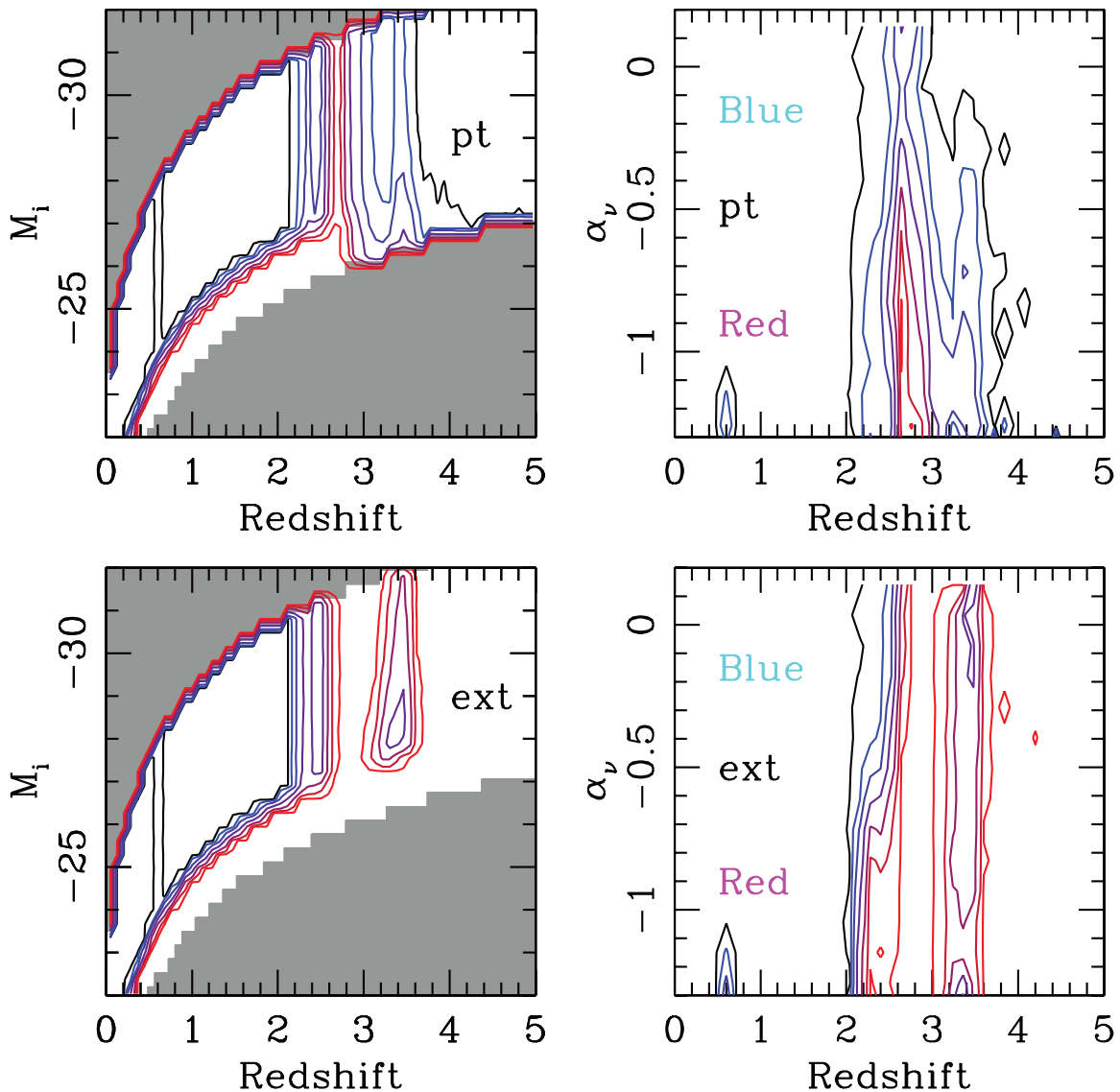
FIG. 7.—Completeness as a function of redshift and M_i (left) and optical spectral index (α_ν; right) for point (pt) and extended (ext) sources. Contours are at 1%, 10%, 25%, 50%, 75%, 90%, and 99% completeness. The 99% completeness limit is shown in black; the 1% limit is shown in red. The left panels are exactly the same as the left panels in Fig. 6 modulo a transformation of the axes. Gray areas indicate regions of parameter space not covered by the simulations. We omit the radio panel, since it is featureless (aside from the flux limits).

such objects (without fatal cosmetic defects) at, e.g., $z \approx 2.7$ with $i \leq 19.1$ should be selected. Thus, the redshift dependence of the ratio of color-selected to radio + color–selected quasars brighter than $i = 19.1$ can be used to check the selection function that we have derived above.

Figure 10 (left) compares the redshift distribution of radio-selected quasars to those that were both radio- and color-selected (using the full DR3Q sample). The radio selection is much smoother and does not show deficits at $z = 2.7$ and 3.5. Figure 10 (right) compares the ratio of these two curves to the results of the simulations shown in Figure 6; the agreement is good, especially in the redshift of the minimum of the selection function, giving us confidence that we have modeled the selection function reasonably. The alternative selection functions have redshift minima that are offset from that of the observed radio-selected ratio.

In principle, we could use the radio-selected quasars to determine the selection function and drop the simulation-based

selection function we derived in § 3.3. However, we do not do so for several reasons:

1. The radio sample is relatively small (2174 quasars), and, in particular, there are not enough radio-selected quasars at $z \gtrsim 4$ to accurately determine our completeness at high redshift, to use smaller redshift bins than are shown in Figure 10, or to explore the selection function simultaneously in redshift and magnitude.

2. The SDSS quasar selection algorithm only targets radio sources (explicitly) as quasar candidates to $i = 19.1$, whereas the color selection goes to $i = 20.2$ for $z > 3$.

3. Several authors have suggested that radio-detected quasars are systematically redder than radio-quiet quasars, even after accounting for the ability of radio selection to uncover dust-reddened quasars (e.g., Ivezić et al. 2002).

4. Finally, the radio and optical redshift distributions may be intrinsically different.
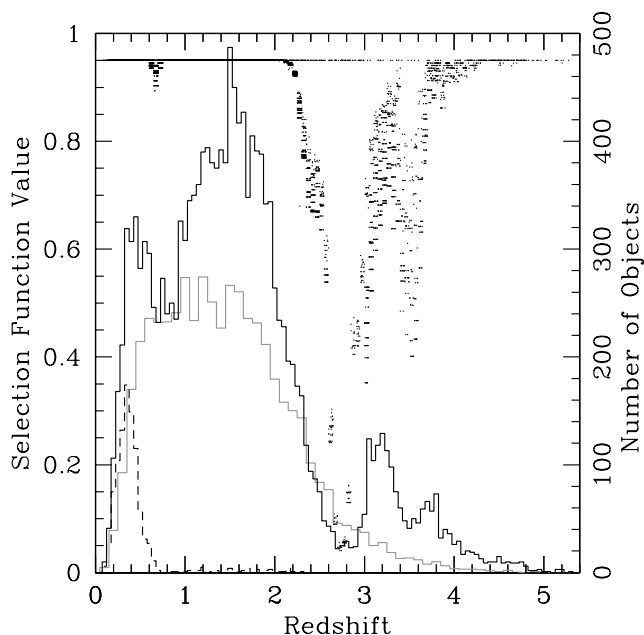
FIG. 8.—Redshift distribution (*black solid line*) of our main quasar sample, together with the correction for each quasar as derived from the selection function for that quasar's redshift and magnitude (Fig. 6). The selection algorithm is quite complete for $z < 2.2$ but suffers from highly redshift-dependent incompleteness at higher redshifts, reaching as low as ∼5% at $z \approx 2.7$. The line of $z \sim 2.7$ quasars with selection function equal to 95% are radio-selected objects. It is not strictly possible to correct the redshift distribution of the full sample shown; however, the gray line shows the redshift distribution after applying an $i = 19.1$ mag cut after correcting for emission-line effects, applying the selection function weights, and removing extended sources. The redshift distribution of extended sources (which may be contaminated by host galaxy light) is shown by the dashed histogram.

FIG. 9.—Raw (*dashed line*) and corrected (*solid line*) redshift histograms for $M_i < -27.6$. This absolute magnitude cut is the faintest for which the SDSS selection function is not truncated by the apparent magnitude limits of the survey. The dotted line and the dot-dashed line show the corrected distribution for two slightly different sets of simulated quasars (and the resulting completeness corrections); see text for discussion. The corrected redshift distribution is much smoother than the observed distribution but is uncertain in the $z = 2.2-3$ range. The (Poisson) error bars are conservative in the sense that they were determined before imposing a floor of 0.333 on the selection function.

4. NUMBER COUNTS

The differential number counts distribution for our statistical sample of quasars is shown in Figure 11. We use the g band, limited to $0.4 < z < 2.1$ and $M_g < -22.5$ ($\alpha_\nu = -0.5$), in order to mimic the final 2QZ/6QZ sample (*squares*; Croom et al. 2004) and the 2SLAQ sample (*triangles*; Richards et al. 2005). At the bright end ($16 < g < 18.5$) we find a slope of 0.99 ± 0.12. Figure 12 presents a similar analysis in the i band for $0.3 < z < 2.2$ and $M_i < -22.5$ [using $M_i(z = 0)$—see § 5—and $\alpha_\nu = -0.5$] and also for $3 < z < 5$. In the range $16 < i < 19$, the $0.3 < z < 2.2$ slope is 0.94 ± 0.09. The cumulative i-band number counts are shown in Figure 13. A least-squares fit between $i = 16$ and 19 yields a slope of 1.01 ± 0.07.[25] The counts have been corrected for cosmetic defect incompleteness and for the redshift- and magnitude-dependent color-selection incompleteness as discussed above. The number counts are also given in tabular form for $0.3 < z < 2.2$ in Table 2 and $3 < z < 5$ in Table 3. In these tables $N(i)$ is the number of quasars per 0.25 mag deg^{-2}, $N(<i)$ is the number of quasars per square degree brighter than magnitude i, N_Q is the number of observed quasars in each 0.25 mag bin, and N_{Qcor} is the number of quasars after correcting for selection effects. For $z < 2.2$ those corrections are negligible.

The cumulative number counts shown in Figure 13 include a data point derived from the 114 quasars found by the PG Bright
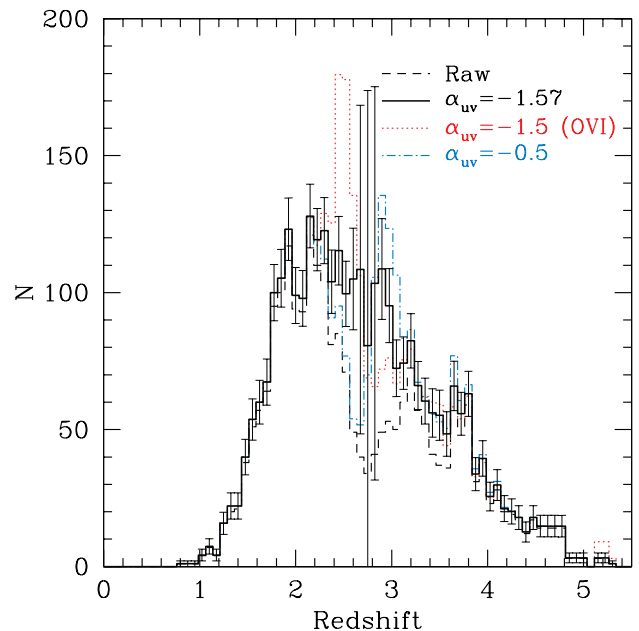
Quasar Survey (BQS; Schmidt & Green 1983) over an area of 10,714 deg^2. We convert the BQS B Vega magnitudes to i-band AB magnitudes as $i = B - 0.14 - 0.287$, where the first correction term shifts from the Vega to the AB system and the second corrects for the different effective wavelengths of the two filters (7470 and 4400 Å), assuming an $\alpha_\nu = -0.5$ power law. The PG data point agrees well with our SDSS number counts relationship, seemingly in contrast with previous claims of incompleteness in the PG survey (Wampler & Ponz 1985; Goldschmidt et al. 1992; Wisotzki et al. 2000). However, both the SDSS and PG points at this magnitude fall below an extrapolation from fainter data points. A combination of incompleteness due to the large photometric errors in the BQS photometry (Jester et al. 2005) and complicated Eddington bias corrections due to the steep local slope of the number counts (as compared to the global average slope) may reconcile the reported incompleteness of the PG sample with the agreement with our number counts (Jester et al. 2005).

5. *K*-CORRECTIONS AND THE CALCULATION OF LUMINOSITIES

In order to compare luminosity functions at different redshifts, we must correct our photometry for the effects of redshift on the portion of the spectrum sampled by a given filter. We use *continuum* luminosities throughout as a measure of the energy output of the central engine, subtracting the contribution of emission lines to the observed flux. This section describes the determination of the *K*-correction, which brings the observed magnitudes to a common effective rest-frame bandpass.

The sign convention of the *K*-correction, $K(z)$, is defined by Oke & Sandage (1968) as $m_{\rm intrinsic} = m_{\rm observed} - K(z)$. The *K*-correction itself depends on the object's SED and is given by

---

[25] Note the discrepancy with the cumulative number counts analysis by Vanden Berk et al. (2005), where the counts of bright quasars appear to be overestimated.
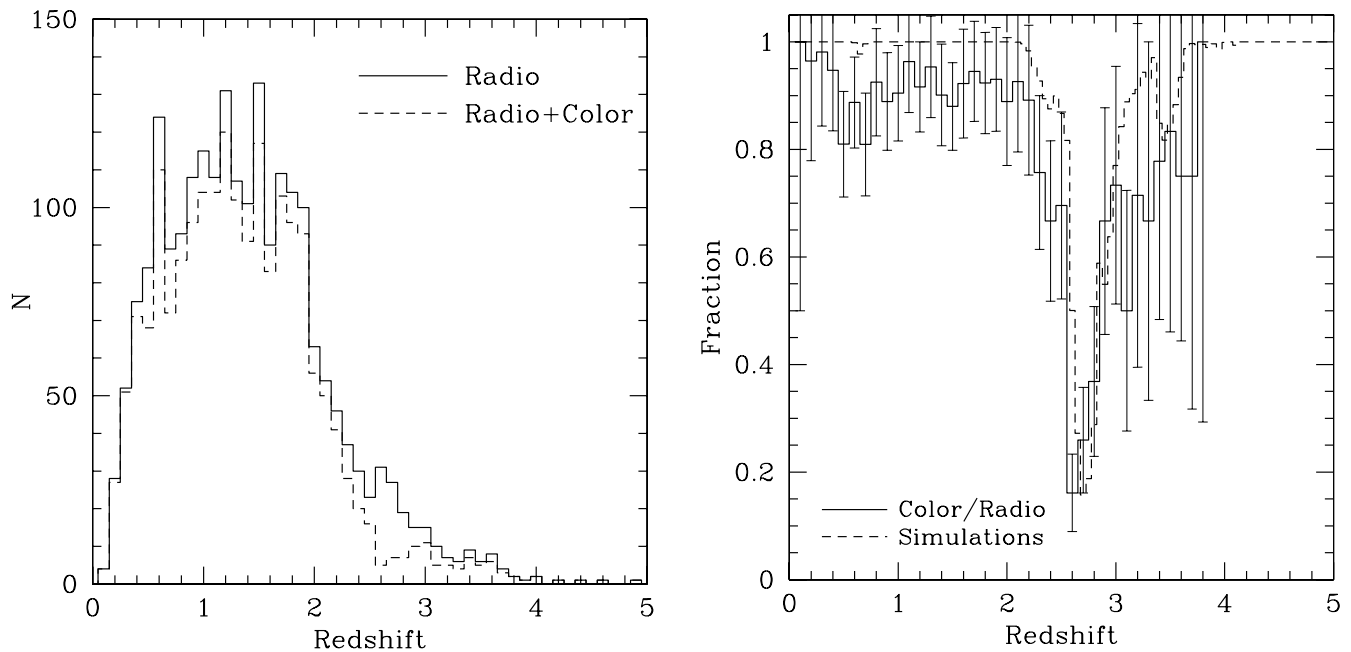
FIG. 10.—*Left*: Redshift distribution of radio-selected (*solid line*) and radio + color–selected (*dashed line*) unresolved DR3 quasars. Note the deficit of color-selected objects at $z \sim 2.7$, where SDSS color selection is difficult. *Right*: Color-selection completeness as a function of redshift determined from the ratio of color- to radio-selected $i \leq 19.1$ quasars (*solid line*) and determined from the simulations (*dashed line*). The depth and position of the dip at $z = 2.7$ are in reasonable agreement between the two determinations. The error bars are Poisson. The fractions derived from the simulations have *not* been corrected for the 5% cosmetic defect incompleteness.

equation (4) in Oke & Sandage (1968) or, equivalently, by equation (8) in Hogg et al. (2002).

While the K-correction depends on the overall quasar SED, we find it useful to consider the component due to the continuum (K_{cont}) and emission lines (K_{em}) separately. This distinction allows us to quantify the sensitivity of the K-correction on the continuum slope, α_ν, and to correct luminosities for the contribution of emis-

sion lines. In particular, the K-correction to $z = 0$ for a power-law continuum is given by $K_{\mathrm{cont}} = -2.5(1 + \alpha_\nu) \log_{10}(1 + z)$, where the first term corrects for the effective narrowing of the filter width with redshift. As emission lines make quasars appear brighter relative to the continuum, K_{em} will be used to *subtract* the emission-line contribution from the observed fluxes.

K-corrections are traditionally defined relative to redshift zero; that is, the photometry of all quasars is referenced to a bandpass
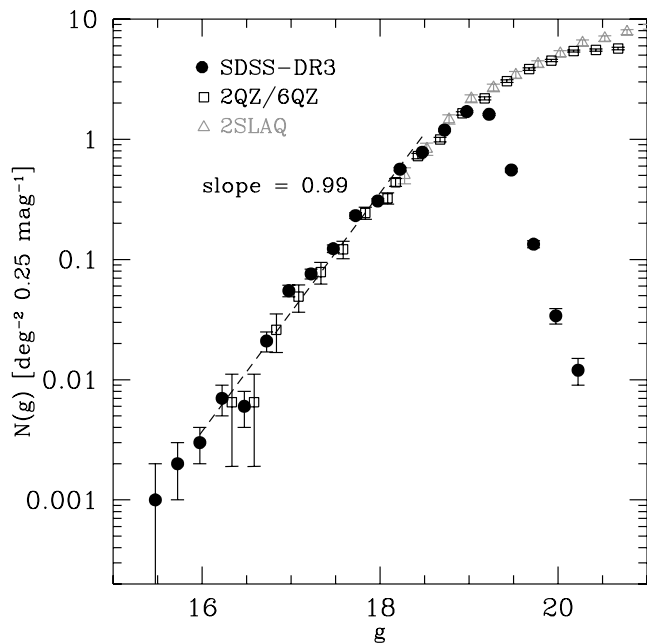

FIG. 11.—Differential g-band number counts for quasars matching the selection criteria of 2QZ ($0.4 < z < 2.1$, $M_g < -22.5$ with a K-correction using a fixed $\alpha_\nu = -0.5$). The 2QZ/6QZ data are shown by squares (assuming $b_J \approx g$); 2SLAQ data are shown by triangles. The falloff at faint magnitudes in the SDSS DR3 sample is due to the i-band limiting magnitude of the survey. Also shown is a power-law fit to the bright end of the SDSS DR3 sample; it has a slope of 0.99 ± 0.12.
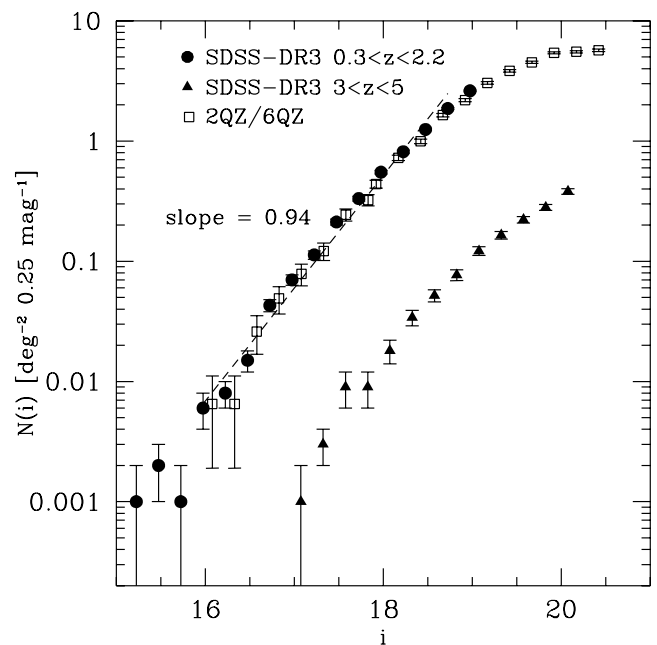

FIG. 12.—Differential i-band number counts with $0.3 < z < 2.2$ (*circles*) and $3 < z < 5$ (*triangles*) (both have $M_i < -22.5$ K-corrected to $z = 0$ with a fixed $\alpha_\nu = -0.5$). The 2QZ/6QZ data are shown by squares and have been converted to i according to $i = g - 0.255$. A power-law fit over the range shown by the dashed line has a slope of 0.94 ± 0.09.
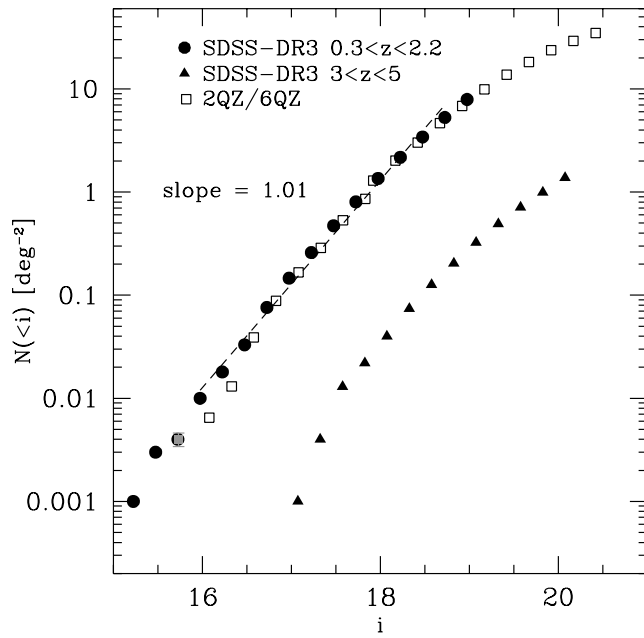
FIG. 13.—Cumulative i-band number counts with $0.3 < z < 2.2$ (circles) and $3 < z < 5$ (triangles) (both have $M_i < -22.5$ and fixed $\alpha_\nu = -0.5$). The 2QZ/6QZ data are shown by open squares and have been converted to i according to $i = g - 0.255$. The gray square represents the cumulative density of PG quasars (Schmidt & Green 1983) with $0.3 < z < 2.2$ and $M_i < -22.5$ assuming $i = B - 0.14 - 0.287$. A power-law fit over the range shown by the dashed line has a slope of 1.01 ± 0.07. Since the errors are correlated, error bars are not shown, but their approximate size can be determined from Fig. 12.

measuring rest-frame optical light. However, low-redshift quasars are very rare, and for the vast majority of the quasars in our sample the K-correction has to extrapolate the observed SED far into the observed infrared. This is problematic, especially because there is a wide range of continuum slopes of quasars. This is illustrated in Figure 14 (top), which shows the difference between the $K_{\rm cont}$ for quasars in our sample, using the canonical $\alpha_\nu = -0.5$, and that determined from the observed relative $g - i$ color (see the discus-

TABLE 3
QUASAR NUMBER COUNTS ($3 < z < 5$)

i	$N(i)$	$N(<i)$	N_Q	$N_{Q{\rm cor}}$
17.075............	0.00 ± 0.00	0.00 ± 0.00	1	1.1
17.325............	0.00 ± 0.00	0.00 ± 0.00	4	4.5
17.575............	0.01 ± 0.00	0.01 ± 0.00	12	14.2
17.825............	0.01 ± 0.00	0.02 ± 0.00	12	14.2
18.075............	0.02 ± 0.00	0.04 ± 0.00	26	29.7
18.325............	0.03 ± 0.01	0.07 ± 0.00	47	55.8
18.575............	0.05 ± 0.01	0.13 ± 0.01	72	83.8
18.825............	0.08 ± 0.01	0.20 ± 0.01	106	124.7
19.075............	0.12 ± 0.01	0.33 ± 0.01	162	197.5
19.325............	0.17 ± 0.01	0.49 ± 0.01	206	268.4
19.575............	0.22 ± 0.01	0.71 ± 0.01	275	360.2
19.825............	0.28 ± 0.02	0.99 ± 0.01	322	455.4
20.075............	0.38 ± 0.02	1.37 ± 0.02	410	617.5

sion by Richards et al. 2003): $\alpha_\nu = -0.5 - \Delta(g - i)/0.508$.[26] At redshift 5, the difference in luminosity between the bluest and reddest objects is more than a factor of 100!

Therefore, in this paper we follow Wisotzki (2000) and Blanton et al. (2003b) and K-correct to a redshift closer to the median redshift of our sample. In most of what follows we use a continuum K-correction calculated for an $\alpha_\nu = -0.5$ power law. Our determination of absolute magnitude is pegged to that of the i band for a quasar at $z = 2$, i.e., with an effective rest wavelength of $\sim$2500 Å (but we need to account for the changing size of the bandpass at $z = 2$ in order to determine the 2500 Å luminosity; see eq. [4]). This is a redshift close to that of the peak of luminous quasar activity, and 2500 Å is also the canonical wavelength used to determine the spectral index between optical and X-rays in quasars (Tananbaum et al. 1979; Strateva et al. 2005). As illustrated in Figure 14 (middle), K-correcting to closer to the median redshift of

---

[26] Quasars with power-law continua of $\alpha_\nu = 0$ and -1 have values of $\Delta(g - i)$ that differ by 0.508.

TABLE 2
QUASAR NUMBER COUNTS ($0.3 < z < 2.2$)

| Magnitude	$N(g)$	$N(<g)$	N_Q	$N(i)$	$N(<i)$	N_Q
15.475..................................	0.00 ± 0.00	0.00 ± 0.00	2	0.00 ± 0.00	0.00 ± 0.00	1
15.725..................................	0.00 ± 0.00	0.00 ± 0.00	3	0.00 ± 0.00	0.00 ± 0.00	3
15.975..................................	0.00 ± 0.00	0.01 ± 0.00	4	0.00 ± 0.00	0.00 ± 0.00	2
16.225..................................	0.01 ± 0.00	0.01 ± 0.00	11	0.01 ± 0.00	0.01 ± 0.00	10
16.475..................................	0.01 ± 0.00	0.02 ± 0.00	10	0.01 ± 0.00	0.02 ± 0.00	12
16.725..................................	0.02 ± 0.00	0.04 ± 0.00	32	0.01 ± 0.00	0.03 ± 0.00	23
16.975..................................	0.06 ± 0.01	0.10 ± 0.01	85	0.04 ± 0.01	0.08 ± 0.01	67
17.225..................................	0.08 ± 0.01	0.17 ± 0.01	117	0.07 ± 0.01	0.15 ± 0.01	107
17.475..................................	0.12 ± 0.01	0.29 ± 0.01	190	0.11 ± 0.01	0.26 ± 0.01	174
17.725..................................	0.23 ± 0.01	0.53 ± 0.01	357	0.21 ± 0.01	0.47 ± 0.01	327
17.975..................................	0.31 ± 0.01	0.83 ± 0.01	472	0.33 ± 0.01	0.80 ± 0.01	511
18.225..................................	0.56 ± 0.02	1.40 ± 0.02	868	0.55 ± 0.02	1.35 ± 0.02	849
18.475..................................	0.78 ± 0.02	2.18 ± 0.02	1202	0.82 ± 0.02	2.17 ± 0.02	1257
18.725..................................	1.19 ± 0.03	3.37 ± 0.03	1839	1.25 ± 0.03	3.42 ± 0.03	1923
18.975..................................	1.70 ± 0.03	5.07 ± 0.03	2620	1.86 ± 0.04	5.28 ± 0.03	2870
19.225..................................	1.61 ± 0.03	6.68 ± 0.03	2484	2.62 ± 0.04	7.90 ± 0.04	4028
19.475..................................	0.56 ± 0.02	7.24 ± 0.02	855	...	...	900
19.725..................................	0.13 ± 0.01	7.37 ± 0.01	206	...	...	216
19.975..................................	0.03 ± 0.01	7.41 ± 0.00	53	...	...	55
20.225..................................	0.01 ± 0.00	7.42 ± 0.00	19	...	...	20
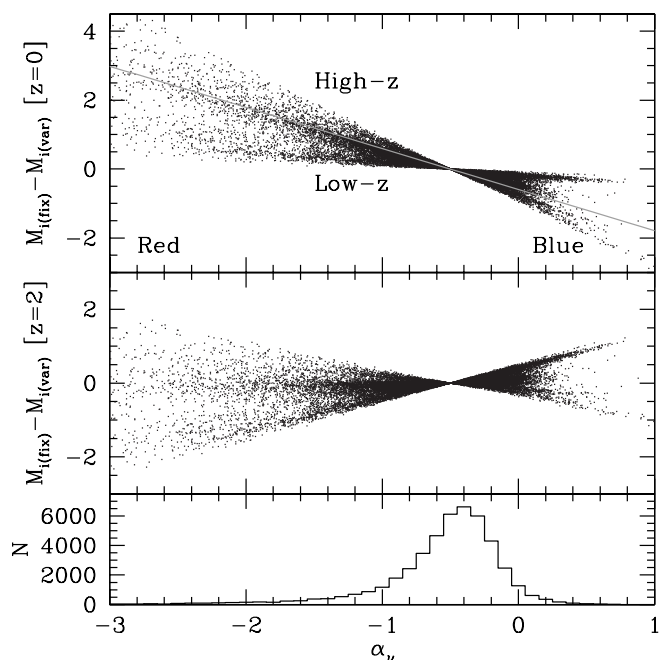
FIG. 14.—Comparison of DR3Q K-corrected absolute i magnitudes computed using both a fixed and a photometrically derived spectral index. The top panel gives the difference for a K-correction normalized to $z = 0$. Note that the bluest and reddest objects at high redshift incur significant errors when using a fixed spectral index for all objects. Moving the zero point of the K-correction to $z = 2$ rotates these points about the $z = 2$ line (*top; gray line*), as can be seen in the middle panel, significantly reducing the systematic error incurred by extrapolating the wrong spectral index to high redshift. Note that these corrections are large only for objects whose spectral indices deviate significantly from the assumed spectral index of $\alpha_\nu = -0.5$; the distribution is shown in the bottom panel.

the sample significantly reduces the systematic error incurred by assuming a constant $\alpha_\nu = -0.5$.

For the emission-line K-correction we proceed as follows. We first construct a variance-weighted mean quasar spectrum from the 16,713 DR1 quasars from Schneider et al. (2003) using the algorithm of Vanden Berk et al. (2001). This spectrum is well fit from Lyα to Hβ by a power law with $\alpha_\nu = -0.436$, in good agreement with the Vanden Berk et al. (2001) composite spectrum. This spectrum shows an appreciably flatter slope longward of Hβ due to contamination from stellar light from quasar hosts at low redshift; this is subtracted off (essentially extrapolating the α_ν power law to longer wavelengths). Next, the continuum is subtracted from the spectrum, and the resulting emission-line spectrum is convolved with the SDSS filter curves to create an emission-line-only K-correction, K_{em}, for each of the filters. Figure 15 shows K_{em} for both the g and i passbands along with K_{cont} for three choices of spectral index. For $z \gtrsim 2.5$ K_{em} for the g band is essentially meaningless as a result of contamination of the continuum by Lyα forest absorption and our uncertainty of the intrinsic continuum shape at wavelengths shorter than Lyα emission (see the discussion in § 3.2). The Lyα forest does not enter the i band until much higher redshift, which is part of the motivation for setting the SDSS quasar selection flux limit in the i band. Table 4 gives our $z = 2$ normalized i-band K-correction vector as a function of redshift for a power-law continuum with $\alpha_\nu = -0.5$ and the emission-line K-correction as discussed above. Comparison of the gray and black lines in Figure 8 demonstrates that the emission-line component of the K-corrections has a significant impact on the true magnitude limit of the sample.

Note that we have *not* corrected the photometry for the presence of host galaxies. At most redshifts we restrict ourselves to
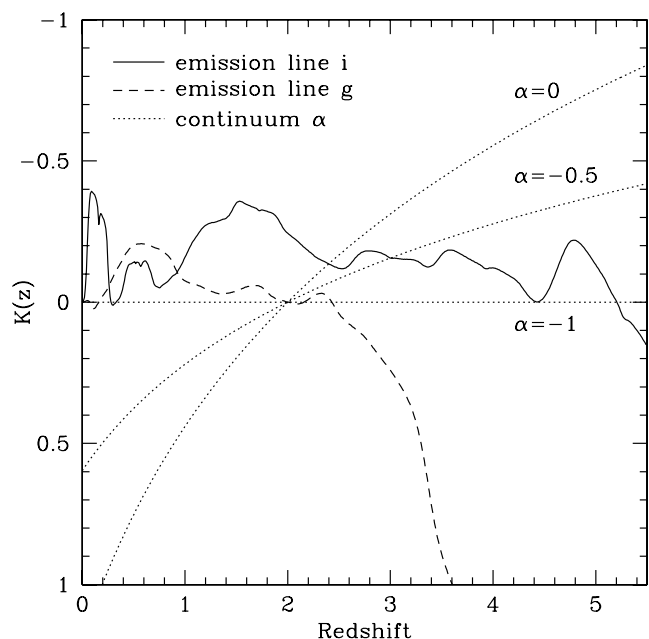

FIG. 15.—Continuum (*dotted lines*) and emission-line (*i: solid line*; *g: dashed line*) K-corrections. The continuum K-corrections are zero at $z = 2$ by definition. For comparison, the i-band K-correction to $z = 0$ for $\alpha_\nu = -0.5$ would be more negative by 0.596 mag.

absolute magnitudes that are several magnitudes brighter than L^* for galaxies; thus, the contribution of host galaxies is likely to be small. We plan to explore this issue in more detail in the future using information on the stellar component from the spectra, when we examine the continuity between quasars and Seyfert galaxies at low redshifts.

Our usage of a $z = 2$ K-corrected i-band magnitude is nonstandard, and it is useful to have a conversion between this and more commonly used magnitudes. First, the conversion between $M_i(z = 0)$ and $M_i(z = 2)$ is given by

$$M_i(z = 0) = M_i(z = 2) + 2.5(1 + \alpha_\nu) \log(1 + 2)$$
$$= M_i(z = 2) + 0.596. \quad (1)$$

For reference, $M_i(z = 2) = -27.2$ for 3C 273. Then to convert from i to g we must account for both the slope of the spectrum

TABLE 4
K-CORRECTIONS

z_{em}	K-Correction
0.00	0.596
0.01	0.587
0.02	0.569
0.03	0.531
0.04	0.462
0.05	0.372
0.06	0.268
0.07	0.203
0.08	0.170
0.09	0.157

NOTES.—The i-band K-corrections, including both the emission-line and continuum ($\alpha_\nu = -0.5$, normalized at $z = 2$) components. Table 4 is published in its entirety in the electronic edition of the *Astronomical Journal*. A portion is shown here for guidance regarding its form and content.
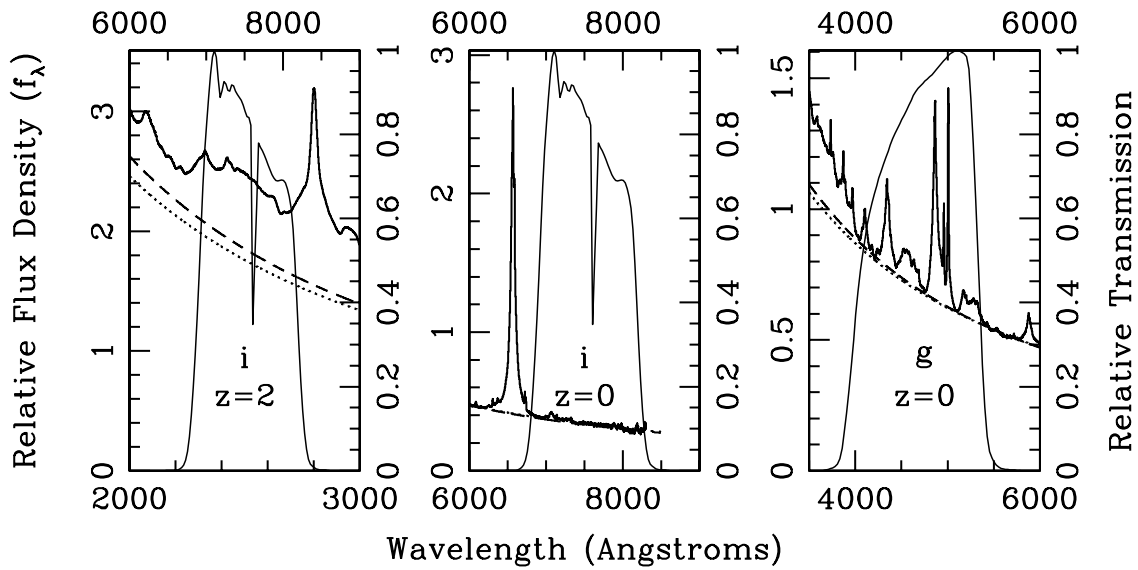
Fig. 16.—Composite quasar spectrum for three different bandpasses: i at $z = 2$, i at $z = 0$, and g at $z = 0$. The composite spectrum is shown by the thick solid lines (relative flux given on the left axes), and the filter curves are shown by the thin solid lines (relative transmission given on the right axes). The bottom axes are rest wavelength, and the top axes are observed wavelength. Dashed and dotted lines represent $\alpha_\nu = -0.436$ and -0.5, respectively. Our K-corrected absolute magnitudes are defined using the $z = 2$ i bandpass shown in the left panel, after excluding the emission-line component above the $\alpha_\nu = -0.436$ continuum.

between i and g and the average emission-line flux in the g band as follows:

$$M_g(z = 0) = M_i(z = 0) + 2.5\alpha_\nu \log\left(\frac{4670 \text{ Å}}{7471 \text{ Å}}\right) - 0.187$$

$$= M_i(z = 0) + 0.255 - 0.187, \quad (2)$$

where $\alpha_\nu = -0.5$ makes quasars 0.255 mag fainter in g than i and emission lines contribute an average of 0.187 mag over $0.3 < z < 2.2$ (including 0.114 mag of flux from emission lines at $z = 0$). Vega-based photometric systems require an additional correction term: $B - g$ is ~ 0.14 (Fukugita et al. 1996). Richards et al. (2005) empirically find that $g - b_J \sim -0.045$; thus, theoretically, we expect $M_{b_J} - M_i(z = 2)$ to be ~ 0.71. Empirically, we determine $M_{b_J} - M_i(z = 2) = 0.66 \pm 0.31$ from a sample of 1046 quasars detected by both SDSS and 2QZ with $0.3 < z < 2.2$ and $i < 19.1$. Finally, assuming a power-law spectral index, the conversion between a monochromatic 1450 Å absolute magnitude and $M_i(z = 2)$ is

$$M_{1450} = M_i(z = 2) + 0.596 + 2.5\alpha_\nu \log\left(\frac{1450 \text{ Å}}{7471 \text{ Å}}\right)$$

$$= M_i(z = 2) + 1.486. \quad (3)$$

Figure 16 illustrates the difference between our K-corrections and a more standard K-correction in terms of the quasar SED. The left panel shows the composite quasar spectrum discussed above at $z = 2$, with the i-band filter curve overplotted. Our $M_i(z = 2)$ absolute magnitude is defined using this bandpass, excluding the mean emission-line component (above the continuum level shown by the dashed line). The middle panel shows the composite spectrum at $z = 0$ relative to the i bandpass; there is essentially no emission-line flux, thus the emission-line component of the K-correction is naturally zero. The right panel shows a more traditional bandpass for absolute magnitudes, the g bandpass at $z = 0$. Traditional systems include the emission-line component in the absolute magnitude definition by defining the $z = 0$ K-correction to be zero.

Finally, to assist in converting between magnitudes and luminosity, we give the conversion from $M_i(z = 2)$ to 2500 Å luminosity density in cgs (ergs s^{-1} Hz^{-1}) following Oke & Gunn (1983):

$$\log\left(\frac{L_{2500 \text{ Å}}}{4\pi d^2}\right) = -0.4[M_i(z = 2) + 48.60 + 2.5 \log(1 + 2)],$$

$$(4)$$

where $d = 10$ pc $= 3.08 \times 10^{19}$ cm and the last term on the right-hand side corrects for the size of the $z = 2$ bandpass relative to a $z = 0$ bandpass [and is needed to convert $M_i(z = 2)$ to physical units in the rest frame]. Our correction for K_{em} means that, on average, this luminosity measures the continuum only and is roughly a nuclear luminosity. In particular, it excludes the *average* contribution from the Balmer continuum and Fe II complexes to the 2500 Å bandpass.

6. LUMINOSITY FUNCTION

We compute the QLF by two methods: by binning the quasars in redshift and luminosity and by using a maximum likelihood (ML) fit to a parameterized form. The input for both of these QLFs is the homogeneous statistical sample of 15,343 quasars drawn from 1622 deg^2. These objects are given in Table 5, which includes the object name, redshift, i-band magnitude (dereddened),

TABLE 5
Statistical Quasar Sample

Name (SDSS J)	z_{em}	i	$M_i(z = 2)$	$\Delta(g - i)$	Cor
000009.26+151754.5	1.199	19.08	−25.40	0.25	0.95
000009.38+135618.4	2.240	18.18	−27.86	0.32	0.93
000011.41+145545.6	0.460	19.09	−23.21	0.01	0.95
000013.14+141034.6	0.949	19.05	−25.02	−0.08	0.95
000024.02+152005.4	0.989	18.99	−25.15	−0.11	0.95

NOTE.—Table 5 is published in its entirety in the electronic edition of the *Astronomical Journal*. A portion is shown here for guidance regarding its form and content.
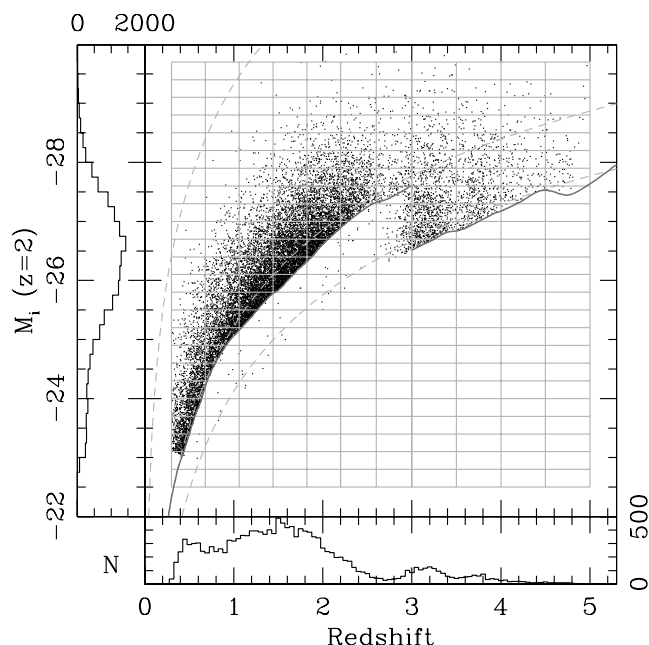
Fig. 17.—Absolute magnitude, $M_i(z=2)$, of the complete sample vs. redshift. The solid light-gray lines show the bins that are used in computing the (binned) luminosity function. Dashed curves show the $i = 15.0$, 19.1, and 20.2 mag limits of the survey (without emission-line K-corrections). The difference between the dashed lines and the solid dark-gray lines shows the effect of the emission-line K-correction. The $z \lesssim 3$ quasars with $i > 19.1$ were selected by the high-z ($griz$) branch of the algorithm and clearly do not represent a complete sample; they are not used in the determination of the QLF. The bottom and side panels show the marginal distributions in redshift and absolute magnitude, respectively.

$M_i(z=2)$, relative color $\Delta(g-i)$, and value of the selection function (Cor).

6.1. The Binned QLF

Figure 17 plots absolute magnitude as a function of redshift for our sample and shows the bins in which the luminosity function is calculated. The edges of the redshift bins are 0.30, 0.68, 1.06, 1.44, 1.82, 2.20, 2.6, 3.0, 3.5, 4.0, 4.5, and 5.0. The M_i bins start at -22.5 and are in increments of 0.3 mag. The dashed curves represent the limiting apparent magnitudes of the survey expressed as a luminosity as a function of redshift, while the solid curves show the effect of subtracting the emission-line component, $K_{em}(z)$.

To compute the binned QLF, we use the Page & Carrera (2000) implementation of the $1/V_{max}$ method (Schmidt 1968; Avni & Bahcall 1980) to correct for bins that intersect the apparent magnitude limits (i.e., incomplete bins). The resulting i-band QLF is shown in Figure 18 (squares); the error bars are given by Poisson statistics. The binned QLF is also given in Table 6, which lists the redshift and absolute magnitude, the log of the space density (Φ) in Mpc^{-3} mag^{-1}, the error in Φ, an indicator of whether the bin is filled, the mean redshift of the quasars in the bin, the number of quasars in the bin, and the weighted number of quasars in the bin. Filled squares in Figure 18 represent complete bins (i.e., those that lie completely above the completeness limit shown in Fig. 17), whereas open squares represent those bins for which we have applied a correction for incomplete coverage of the bin. Corrections for cosmetic defects and color selection as a function of redshift and magnitude have been applied.

6.2. Choosing a ML Form

We have also determined the luminosity function as derived from a ML analysis that requires no binning. The likelihood

function is calculated using equation (22) of Fan et al. (2001; see also Marshall 1985) and is maximized using Powell's method (Press et al. 1992). The ML solution is shown in Figure 18 (dashed line); our choice of parameterization is discussed below.

The QLF is often parameterized by a standard double power-law form (e.g., Pei 1995; Peterson 1997; Boyle et al. 2000; Croom et al. 2004):

$$\Phi(M, z) = \frac{\Phi(M^*)}{10^{0.4(\alpha+1)(M-M^*)} + 10^{0.4(\beta+1)(M-M^*)}}, \quad (5)$$

where $\Phi(M, z)dM$ is the number of quasars per unit comoving volume at redshift, z, with absolute magnitudes between $M - dM/2$ and $M + dM/2$. This is the standard form for deep quasar surveys, which generally find a flatter slope fainter than some characteristic luminosity. However, the SDSS quasar survey, while covering a very large area of sky, is actually quite shallow. The limiting magnitude is such that, at most redshifts, the SDSS does not observe objects fainter than the "break" characteristic luminosity, and a double power-law form is not justified. While there is some curvature in the shape of the QLF and our low-redshift data would be better fit by a double power-law form, overall the luminosity coverage is not broad enough to justify the added parameter.

Boyle et al. (2000) and Croom et al. (2004) use the 2QZ data to show that the redshift evolution of luminous $z \lesssim 2.2$ quasars can be parameterized by PLE, whereby M^* is either a quadratic in redshift or an exponential function of look-back time. However, neither of these forms is appropriate for a QLF that extends to higher redshifts. The space density is seen to fall for $z > 2.5$ (Osmer 1982; Schmidt et al. 1995; Kennefick et al. 1995; Fan et al. 2001), while the exponential form rises with z. The quadratic form properly falls with z, but it assumes a fall that is symmetric with the rise from $z = 0$ to $z \sim 2$, while the data exhibit a less steep decline in redshift (the decline is much steeper for $z > 2$ when considering look-back time). As such, we cannot use the traditional PLE parameterizations.

Thus, a hybrid form is required. Indeed, X-ray surveys have recently begun to use a luminosity-dependent density evolution (LDDE) parameterization to describe the X-ray QLF (Schmidt & Green 1983; Ueda et al. 2003). Such a parameterization allows the redshift of the peak quasar density to change as a function of luminosity (as seems to be required by the X-ray data).

Figure 19 illustrates the complexity of choosing a functional form for the QLF for a luminous quasar sample spanning $0 < z < 5$ by showing what happens when one naively extrapolates the forms used or derived by Wolf et al. (2003), Richards et al. (2005), Ueda et al. (2003), Croom et al. (2004), Barger et al. (2005), Hunt et al. (2004), Meiksin (2005), and Hasinger et al. (2005). We have followed Richards et al. (2005) to convert between X-ray and optical luminosity functions. All of the parameterizations are extended well beyond the data that were used to construct them, and there is a considerable degree of ambiguity in the transformations; thus, this comparison is intended to be illustrative only. This presentation is not meant to belittle the accuracy of these models, but rather to show that existing parameterizations do not generally provide an accurate description of the redshift evolution of luminous quasars simultaneously at low and high redshift. In particular, surveys with relatively small areas are expected to predict QLF slopes that are too flat when extrapolated to higher luminosities at low redshift. This flattening occurs as a result of the intrinsic flattening of the QLF at luminosities at which the majority of the sources are found (deep, pencil-beam surveys having fainter mean luminosities than shallow, wide-area surveys).
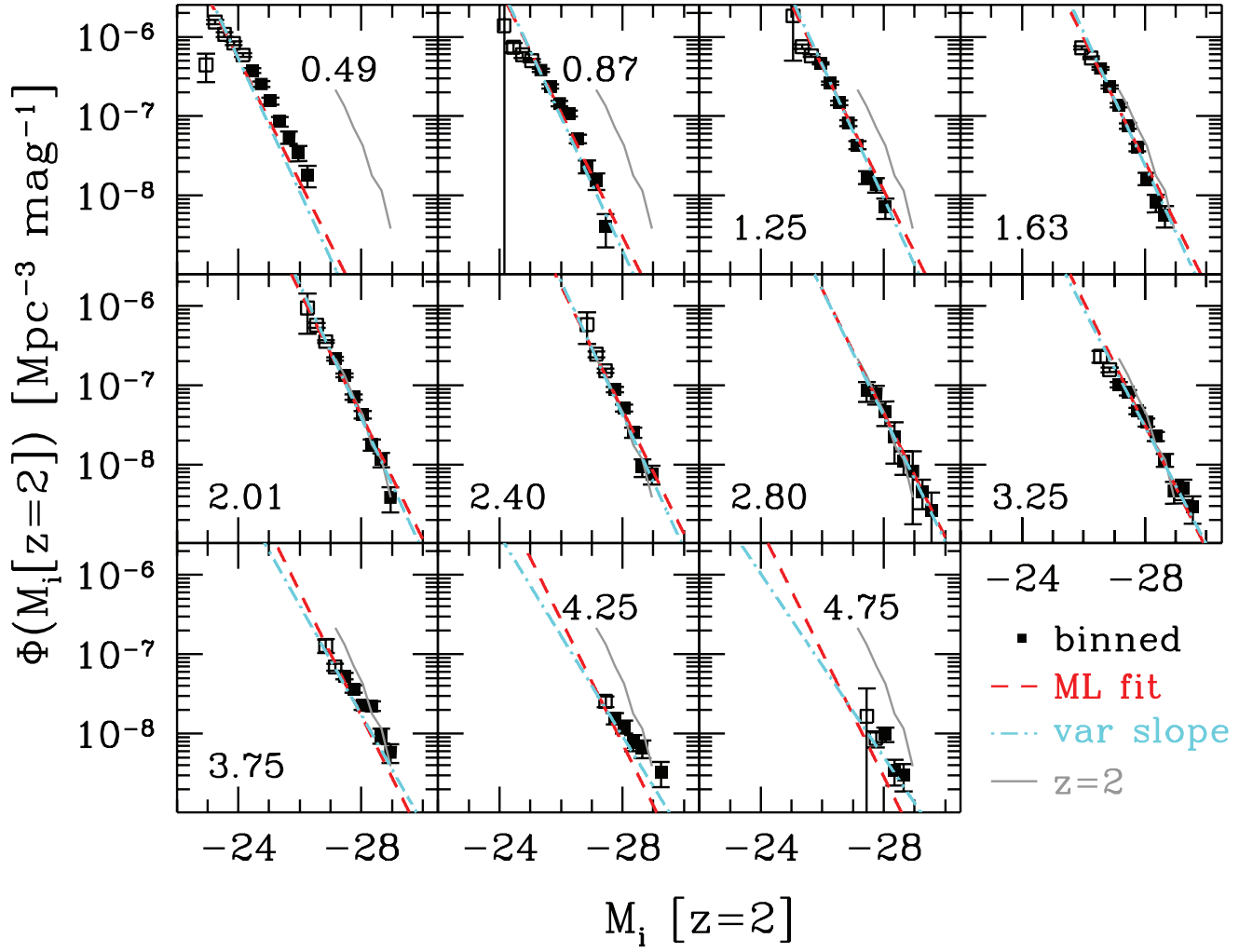
Fig. 18.—$M_i(z = 2)$ luminosity function (roughly a 2500 Å luminosity; see eq. [4]). The redshift of each slice is given in the top right or bottom left corner of each panel. The squares show the binned luminosity function using a $1/V_{max}$ method; open squares are incomplete bins. The $z = 2.01$ curve (*gray line*) is reproduced in each panel for the sake of comparison. The dashed line is our best-fit ML parameterization assuming a constant slope with redshift, while the dot-dashed line allows for a slope change at high redshift. Corrections for cosmetic defects and color selection as a function of redshift and magnitude have all been applied. Note that there is almost no overlap in absolute magnitude between the highest and lowest redshift bins.

6.3. The ML QLF

In this work we have chosen to determine the ML solution with respect to a PLE form similar to that of Wolf et al. (2003), specifically,

$$\Phi = \Phi^* 10^{A_1 \mu}, \qquad (6)$$

where

$$\mu = M - (M^* + B_1 \xi + B_2 \xi^2 + B_3 \xi^3), \qquad (7)$$

and

$$\xi = \log\left(\frac{1 + z}{1 + z_{ref}}\right). \qquad (8)$$

In these equations Φ^*, A_1, B_1, B_2, and B_3 are free parameters, z_{ref} has been set to 2.45, and M^* has been set to -26. This form differs from Wolf et al. (2003) only in that it lacks a second-

order A term, which is not justified by the dynamic range of our data. At any given redshift, this luminosity function is a single power law: $\Phi(L) \propto L^\beta$, where $\beta = -(2.5A_1 + 1)$. For a single power-law luminosity function, there is no difference between PLE and pure density evolution (PDE), as there is no characteristic scale in luminosity. The best-fit values and their uncertainties from our ML analysis are given in the first row of Table 7. Our value of A_1 corresponds to a bright-end slope in the Croom et al. (2004) parameterization of $\beta = -2.95$ ($A_1 = 0.78$). This form does reasonably well at describing the overall redshift and luminosity evolution of the quasars in our sample; see Figure 18 (*dashed line*). However, the χ^2 of this ML fit (as compared to the binned QLF) is 394 for 69 degrees of freedom, suggesting that a more accurate parameterization is still needed.

Figure 20 shows the space density of luminous quasars (i.e., the integral of the QLF). This shows the familiar peak at $z \approx 2.5$; at much lower and higher redshifts, luminous quasars are very rare indeed. The exact redshift of the peak is uncertain, a situation exacerbated by the large and uncertain incompleteness in our sample at $z \approx 2.7$. Note the good agreement between our space density evolution and that of previous papers. In particular,

TABLE 6

BINNED QUASAR LUMINOSITY FUNCTION

z (1)	$M_i(z=2)$ (2)	$\log \Phi$ (3)	$\sigma_\Phi(\times 10^{-9})$ (4)	Fill (5)	$\bar{z}$ (6)	N_Q (7)	$N_{Q\mathrm{cor}}$ (8)
0.49	−26.25	−7.74	5.48	1	0.59	11	11.6
0.49	−25.95	−7.46	7.55	1	0.58	21	22.2
0.49	−25.65	−7.26	9.47	1	0.58	33	34.8
0.49	−25.35	−7.07	11.90	1	0.55	52	54.9
0.49	−25.05	−6.81	16.01	1	0.56	94	99.3
0.49	−24.75	−6.59	20.52	1	0.58	154	163.0
0.49	−24.45	−6.42	24.94	1	0.57	228	241.0
0.49	−24.15	−6.23	35.98	0	0.54	337	358.2
0.49	−23.85	−6.08	43.96	0	0.51	358	377.2
0.49	−23.55	−5.97	75.48	0	0.45	311	331.3
0.49	−23.25	−5.81	102.81	0	0.41	290	307.2
0.49	−22.95	−6.35	174.24	0	0.41	39	46.9
0.87	−27.45	−8.39	1.81	1	0.95	5	5.3
0.87	−27.15	−7.81	3.53	1	0.95	19	20.0
0.87	−26.85	−7.63	4.36	1	0.95	29	30.5
0.87	−26.55	−7.29	6.48	1	0.94	64	67.4
0.87	−26.25	−6.96	9.38	1	0.91	134	141.2
0.87	−25.95	−6.84	10.84	1	0.92	179	188.5
0.87	−25.65	−6.62	13.87	1	0.92	293	308.6
0.87	−25.35	−6.42	17.57	1	0.93	470	495.1
0.87	−25.05	−6.30	24.49	0	0.89	492	520.0
0.87	−24.75	−6.23	51.36	0	0.78	284	307.6
0.87	−24.45	−6.13	100.79	0	0.73	122	133.7
0.87	−24.15	−5.86	1446.59	0	0.74	9	13.8
1.25	−28.05	−8.15	2.06	1	1.31	12	12.6
1.25	−27.75	−7.86	2.85	1	1.32	23	24.2
1.25	−27.45	−7.76	3.20	1	1.27	29	30.5
1.25	−27.15	−7.36	5.07	1	1.30	73	76.8
1.25	−26.85	−7.08	7.00	1	1.30	139	146.3
1.25	−26.55	−6.83	9.37	1	1.29	249	262.1
1.25	−26.25	−6.58	12.44	1	1.29	439	462.1
1.25	−25.95	−6.33	16.62	1	1.28	783	824.2
1.25	−25.65	−6.24	22.56	0	1.23	733	773.5
1.25	−25.35	−6.12	48.01	0	1.13	360	382.8
1.25	−25.05	−5.74	1332.39	0	1.09	12	14.6
1.63	−28.65	−8.25	1.70	1	1.66	11	11.6
1.63	−28.35	−8.08	2.06	1	1.67	16	16.8
1.63	−28.05	−7.78	2.91	1	1.68	32	33.7
1.63	−27.75	−7.39	4.57	1	1.66	79	83.2
1.63	−27.45	−7.12	6.23	1	1.67	147	154.7
1.63	−27.15	−6.86	8.43	1	1.66	269	283.2
1.63	−26.85	−6.63	10.94	1	1.65	453	476.8
1.63	−26.55	−6.40	14.35	1	1.66	779	820.0
1.63	−26.25	−6.26	19.09	0	1.62	892	940.9
1.63	−25.95	−6.14	38.86	0	1.52	477	506.0
2.01	−28.95	−8.41	1.37	1	1.99	8	8.4
2.01	−28.65	−7.94	2.37	1	2.02	24	25.3
2.01	−28.35	−7.75	2.94	1	2.02	37	39.0
2.01	−28.05	−7.37	4.53	1	2.01	88	92.7
2.01	−27.75	−7.15	5.86	1	2.03	147	155.0
2.01	−27.45	−6.87	8.03	1	2.02	276	291.0
2.01	−27.15	−6.67	10.22	1	2.01	447	471.1
2.01	−26.85	−6.45	13.97	0	1.99	648	682.7
2.01	−26.55	−6.24	40.12	0	1.90	430	464.3
2.01	−26.25	−6.03	495.10	0	1.87	30	39.4
2.40	−28.95	−8.12	2.07	1	2.44	14	17.9
2.40	−28.65	−8.03	2.30	1	2.41	17	21.8
2.40	−28.35	−7.59	3.71	1	2.37	48	59.7
2.40	−28.05	−7.29	5.28	1	2.37	98	121.2
2.40	−27.75	−7.05	7.01	1	2.37	164	208.1
2.40	−27.45	−6.82	9.50	0	2.38	265	356.0
2.40	−27.15	−6.61	22.11	0	2.30	246	309.0
2.40	−26.85	−6.24	249.51	0	2.25	37	48.8
2.80	−29.55	−8.57	1.76	1	2.70	3	6.2

TABLE 6—Continued

z (1)	$M_i(z=2)$ (2)	$\log \Phi$ (3)	$\sigma_\Phi(\times 10^{-9})$ (4)	Fill (5)	$\bar{z}$ (6)	N_Q (7)	$N_{Q\mathrm{cor}}$ (8)
2.80	−29.25	−8.34	1.84	1	2.82	7	10.6
2.80	−28.95	−8.08	6.51	1	2.82	10	19.2
2.80	−28.65	−7.95	3.68	1	2.80	12	25.9
2.80	−28.35	−7.65	11.94	1	2.83	24	51.5
2.80	−28.05	−7.33	15.75	1	2.81	50	107.9
2.80	−27.75	−7.11	20.63	1	2.82	75	180.1
2.80	−27.45	−7.07	24.17	1	2.79	73	199.8
3.25	−29.55	−8.54	1.10	1	3.35	7	8.2
3.25	−29.25	−8.30	1.45	1	3.25	12	14.2
3.25	−28.95	−8.33	1.40	1	3.20	11	13.1
3.25	−28.65	−7.94	2.18	1	3.25	28	32.5
3.25	−28.35	−7.64	3.12	1	3.23	54	64.6
3.25	−28.05	−7.47	3.89	1	3.25	77	95.9
3.25	−27.75	−7.32	4.72	1	3.24	103	134.3
3.25	−27.45	−7.09	6.47	1	3.21	161	228.8
3.25	−27.15	−6.99	7.48	1	3.22	191	287.9
3.25	−26.85	−6.80	10.40	0	3.20	234	377.5
3.25	−26.55	−6.63	39.58	0	3.11	52	103.7
3.75	−28.95	−8.24	1.56	1	3.69	14	15.7
3.75	−28.65	−8.02	2.03	1	3.67	22	25.7
3.75	−28.35	−7.65	3.06	1	3.77	54	60.5
3.75	−28.05	−7.64	3.11	1	3.76	55	62.1
3.75	−27.75	−7.44	4.07	1	3.74	83	99.3
3.75	−27.45	−7.27	4.96	1	3.76	119	144.2
3.75	−27.15	−7.16	6.59	0	3.72	117	158.4
3.75	−26.85	−6.89	25.48	0	3.59	27	54.6
4.25	−29.25	−8.48	1.16	1	4.25	8	8.4
4.25	−28.65	−8.18	1.64	1	4.22	16	16.9
4.25	−28.35	−8.11	1.79	1	4.19	19	20.0
4.25	−28.05	−7.91	2.26	1	4.21	30	31.8
4.25	−27.75	−7.81	2.53	1	4.24	38	40.2
4.25	−27.45	−7.59	3.84	0	4.16	44	47.1
4.75	−28.65	−8.52	1.14	1	4.66	7	7.4
4.75	−28.35	−8.46	1.22	1	4.71	8	8.4
4.75	−28.05	−8.00	2.07	1	4.66	23	24.2
4.75	−27.75	−8.06	1.94	0	4.66	20	21.1
4.75	−27.45	−7.78	20.57	0	4.62	6	8.3

NOTES.—Columns are (1) redshift, (2) $M_i(z=2)$, (3) Φ (Mpc^{-3} mag^{-1}), (4) σ_Φ, (5) an indicator of whether the bin is completely covered by data (1 if yes, 0 if no), (6) the mean redshift of quasars in the bin, (7) the number of quasars in the bin, and (8) the corrected number of quasars in that bin after applying the selection function. Table 6 is also available in machine-readable form in the electronic edition of the *Astronomical Journal*.

extrapolating the $z = 3-5$ trend reveals good agreement with the $z = 6$ point from Fan et al. (2004), but we caution that our functional forms should not be used beyond the $z \sim 5$ limits of our data, as they are cubic fits that diverge quickly.

6.4. Redshift Evolution of the Slope

Schmidt et al. (1995) and Fan et al. (2001) showed that the slope of the $z > 4$ QLF has a value of $\beta = -2.5$, much shallower than that seen for $z < 2.2$ quasars, which typically exhibit a slope of $\beta \sim -3.3$ (Croom et al. 2004). Indeed, this flattening is also apparent in our data. If we fit a line to the $M_i < -25$ binned luminosity function data (to avoid the curvature at the faint end at low redshift) as a function of redshift, we find the slopes given in Figure 21. For $z \leq 2.4$ the slopes are roughly constant to within the errors; a ML fit yields $\beta = -3.1$ ($A_1 = 0.84$). However, at higher redshifts, if we ignore the poorly constrained slope at $z = 4.75$, there appears to be a flattening with redshift.
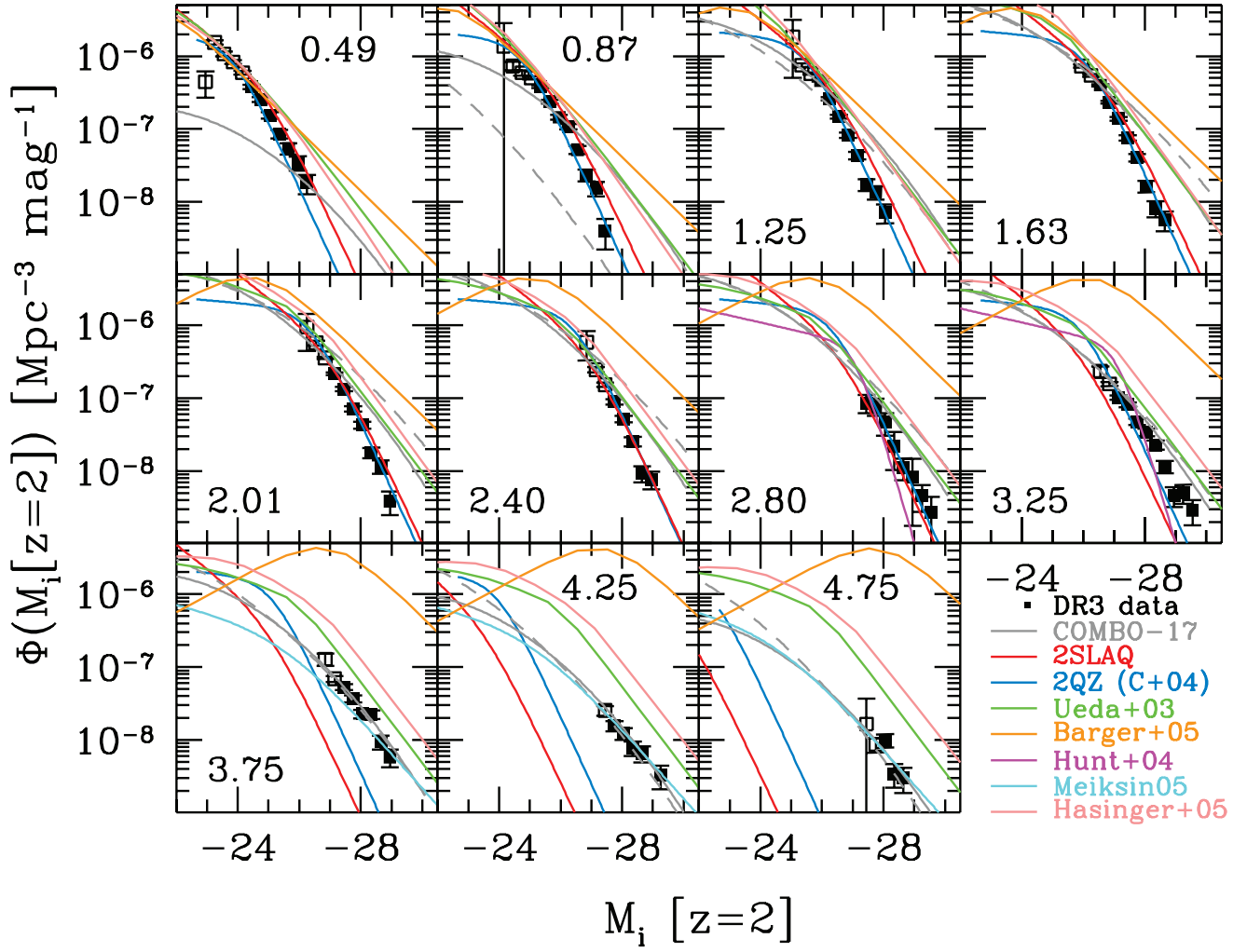
Fig. 19.—Comparison with other QLFs used/derived by COMBO-17 (Wolf et al. 2003; PLE, *solid gray lines*; PDE, *dashed gray lines*), 2SLAQ (Richards et al. 2005; PLE, *red lines*), 2QZ (Croom et al. 2004; PLE, *blue lines*), Ueda et al. (2003; X-ray, LDDE, *green lines*), Barger et al. (2005; X-ray, PLE, *orange lines*), Hunt et al. (2004; *magenta lines*), Meiksin (2005; *cyan lines*), and Hasinger et al. (2005; LDDE, *pink lines*). See Richards et al. (2005) for the conversion between X-ray and optical luminosity functions. All of the parameterizations are extended considerably beyond the data that were used to construct them; this presentation merely emphasizes the difficulty of parameterizing such a large range in luminosity and redshift. The Ueda et al. (2003) parameterization appears to do the best over the full redshift range but does not follow the observed slope change with redshift.

Therefore, we have also attempted to allow for variation in slope in our functional form. To accomplish this we add an $A_2(z - 2.45)$ term to the exponent in equation (6), such that

$$\Phi = \Phi^* 10^{\mu[A_1 + A_2(z - 2.45)]}. \qquad (9)$$

Since the change in slope at high redshift does not appear to extend to lower redshifts, we allow the slope to vary linearly only for $z > 2.4$, fixing the slope to $\beta = -3.1$ for lower redshifts. The second and third rows of Table 7 show the resulting

best-fit values of the free parameters, which show that β flattens to $\gtrsim -2.37$ by $z = 5$. The result of this parameterization is shown in Figure 18 (*dot-dashed line*) and in Figure 20 (*blue line*).

Adding these two parameters (A_2 and the explicit decision of the redshift at which to break the functional form) reduces the χ^2 by 123, a highly significant change. However, the χ^2 per degree of freedom is still 4; this functional form does not fit the data perfectly. Figure 18 reveals that much of the excess χ^2 comes from the poor fit at $z < 1$ (where we are probing faint enough to

TABLE 7
SUMMARY OF MAXIMUM LIKELIHOOD FITS

Form	A_1	A_2	B_1	B_2	B_3	M^*	z_{ref}	$\log \Phi^*$	χ^2	ν
Fixed power law	0.78 ± 0.01	...	0.10 ± 0.04	27.35 ± 0.10	19.27 ± 0.25	-26	2.45	-5.75	394	69
Variable power law ($z > 2.4$)	0.83 ± 0.01	-0.11 ± 0.01	1.43 ± 0.04	36.63 ± 0.10	34.39 ± 0.26	-26	2.45	-5.70	271	67
Variable power law ($z \leq 2.4$)	0.84	0.00	1.43 ± 0.04	36.63 ± 0.10	34.39 ± 0.26	-26	2.45	-5.70	271	67

NOTES.—The fixed power-law model is given by eqs. (6)–(8). See eq. (9) and § 6.4 for the variable power-law model. In this table Φ is in units of Mpc^{-3} mag^{-1}, and M^* and z_{ref} are not free parameters; rather, they are defined to have the values indicated.
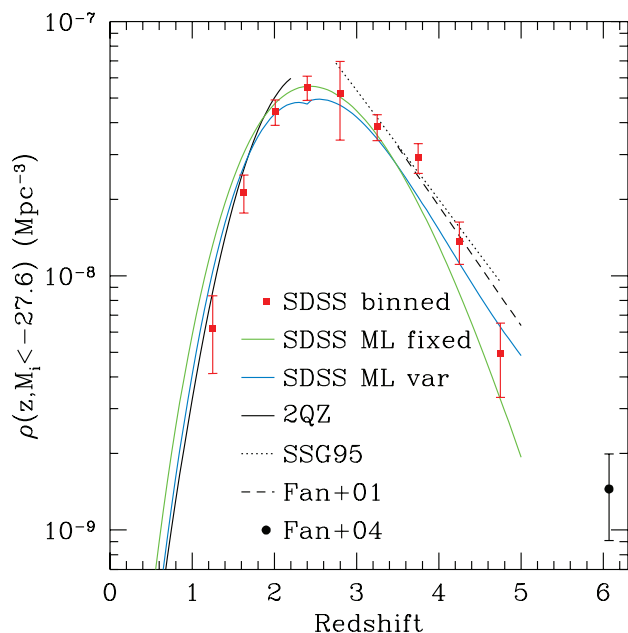
FIG. 20.—Integrated *i*-band luminosity function to $M_i(z = 2) = -27.6$. The solid black line is from 2QZ (Boyle et al. 2000). The squares are from the binned SDSS DR3 QLF. The green and blue lines are from the fixed slope and variable high-redshift slope ML parameterizations of the SDSS DR3 QLF, respectively. The dashed and dotted lines are from Fan et al. (2001; *Fan+01*) and Schmidt et al. (1995; SSG95). The $z \sim 6$ point from Fan et al. (2004; *Fan+04*), converted to our units and cosmology, is shown by the circle. We caution that our ML fits should not be used beyond $z = 5$, as they are cubic fits and quickly diverge beyond the limits of our data.

FIG. 21.—Slope of the binned QLF as a function of redshift determined from a linear least-squares fit to the (complete) $M_i(z = 2) < -25$ points. The slope of the luminosity function significantly flattens with redshift at $z > 3$ (the seemingly discrepant point at $z = 4.75$ was determined from only three luminosity bins and has a large uncertainty). The dashed line shows the best-fit constant slope for $z \leq 2.4$ and the best-fit redshift-dependent slope for $z > 2.4$.

see unmodeled curvature in the QLF and possibly host galaxy contamination).

A more appropriate measure of the improvement of the fit is the amount by which the quantity that is being minimized changes. A 1σ change in a single variable will change the ML parameter by unity, whereas our change of parameterization reduces the value by 102; thus, the added complexity in the parameterization is justified.

Finally, we reiterate the point made by Wisotzki (2000) that the measured slope is sensitive to the extrapolation of the *K*-correction. The *K*-corrections normalized to $z = 0$ and using a fixed spectral index cause the slope of the high-redshift QLF to appear steeper than it should, since the presumed absolute magnitude distribution is narrower than the true distribution. Our use of a $z = 2$ normalized *K*-correction helps to alleviate this problem and highlights the slope change at high redshift. Gravitational lensing can also change the observed slope of the high-redshift QLF (Schneider et al. 1992); however, Richards et al. (2004b, 2006) have used *Hubble Space Telescope* imaging of $z > 4$ SDSS quasars to put limits on this effect.

7. DISCUSSION AND CONCLUSIONS

One of the most interesting results to come out of recent AGN surveys is the evidence in favor of "cosmic downsizing," wherein the peak of AGN activity occurs at higher redshifts for more luminous objects than less luminous objects (Cowie et al. 2003; Ueda et al. 2003; Merloni 2004; Barger et al. 2005). Comparison of X-ray, infrared, and optical surveys requires careful consideration of the fact that many groups find that the ratio of obscured (type 2) to unobscured (type 1) AGNs is inversely correlated with AGN luminosity (e.g., Lawrence 1991; Ueda et al. 2003; Hao
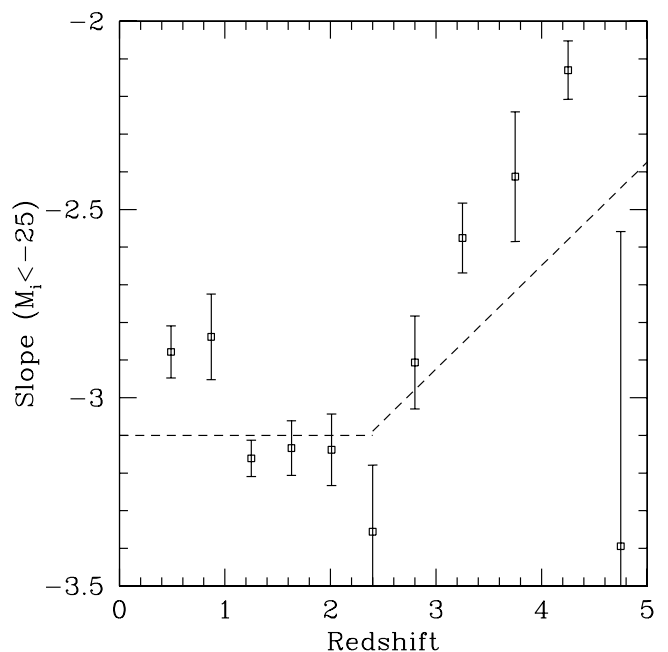
et al. 2005a; but see Treister & Urry 2005). Ignoring this effect and examining the most uniform luminous sample that we can form over the largest redshift range ($M_i < -27.6$), Figure 20 shows that the peak in type 1 quasar activity occurs between $z = 2.2$ and 2.8. Unfortunately, this redshift range is the least sensitive in the SDSS and subject to large error (see Fig. 9). A substantial observing campaign for $z \sim 2.5$ quasars that are buried in the stellar locus (i.e., a sample with close to unity selection function in this redshift region) is needed to resolve this issue. To this end Chiu (2004) and Jiang et al. (2006) describe complete (i.e., not sparsely sampled) surveys of quasars in the mid-z range to address this problem. In addition, near-infrared selected samples such as can be obtained from *Spitzer Space Telescope* photometry should be able to better isolate the peak redshift of luminous type 1 quasars (Brown et al. 2006).

Our most interesting result is the flattening of the slope of the QLF with increasing redshift. This flattening has been demonstrated before using small samples of high-z quasars (Schmidt et al. 1995; Fan et al. 2001), but never so robustly and over such a large redshift range as with these data. While there is little overlap in luminosity between the lowest and highest redshift data (deeper surveys at high redshift are clearly needed), previous constraints on the QLF and the presumption that the QLF will be well-behaved outside of the regions explored (e.g., that the slope does not get *steeper* for faint high-redshift quasars) suggests that the slope change is due to redshift and not luminosity. Small area samples such as the most sensitive hard X-ray surveys (Ueda et al. 2003; Barger et al. 2005) and the COMBO-17 survey (Wolf et al. 2003) primarily probe the low-luminosity end of the QLF, where the slope is flatter; thus, it is not surprising that they systematically find flatter slopes (see Fig. 19). Our confirmation of the flattening of the high-redshift slope has significant consequences in terms of our understanding of the formation and evolution of active galaxies, particularly in light of the popularity of recent models invoking kinetic and radiative AGN feedback in

the evolution of galaxies (e.g., Silk & Rees 1998; Fabian 1999; Wyithe & Loeb 2003; Hopkins et al. 2005).

A particularly interesting explanation for the steepness of the low-redshift QLF comes from the model of Wyithe & Loeb (2003). In their scenario, the predicted slope at low redshift is much flatter than the observed slope (see Fig. 1 of Wyithe & Loeb 2003) for the most luminous quasars. They argue that the so-called break between less and more luminous quasars for $z \lesssim 2$ is the result of "the inability of gas to cool inside massive dark matter halos," thus preventing the formation of $v_c \gtrsim 500 \text{ km s}^{-1}$ galaxies and their resulting luminous quasars in the most massive dark matter halos. Such an idea may be in conflict with the work of Hopkins et al. (2006), who find that the break in the QLF occurs naturally in their models. In their case the break occurs at the maximum of a (roughly) lognormal peak luminosity distribution with more luminous quasars accreting near Eddington and less luminous quasars perhaps accreting at lower rates. However, in both the Wyithe & Loeb (2003) and Hopkins et al. (2006) PLE models the predicted slopes for luminous quasars are actually *steeper* at high redshift than at low redshift (see Fig. 1 in Wyithe & Loeb [2003] and Fig. 11 in Hopkins et al. [2006]), *opposite of that which we observe*. In the case of Hopkins et al. (2006), the evolution to high redshift is determined simply by adjusting the break luminosity of their $0 < z < 3$ model to fit the existing high-redshift data. Thus, to match our observed flattening at high redshift, Hopkins et al. (2006) will either need to change their model or (at the very least) the details of its extrapolation to higher redshift. To explain a flatter QLF slope at high redshift in their model, one would need to invoke a broader distribution of quasar peak luminosities at high redshifts than low, with relatively more low-luminosity objects at low redshift than high. Thus, our observations and future observations of even fainter type 1 quasars at $z > 3$ provide an important litmus test for models of galaxy evolution.

While our analysis was based on over 15,000 quasars, to form this uniform sample we were forced to drop over half of the objects in the DR3 because of inhomogeneity in the selection algorithms. Data Release 5 of the SDSS, which is planned to occur in mid-2006, will contain more than twice as many "new" quasars as are in our DR3 uniform sample. We can define appreciably larger samples, using the photometric selection and photometric redshift techniques of Richards et al. (2004a) and Weinstein et al. (2004); such methods will result in a sample approaching 1 million quasars probing appreciably further down the luminosity function, albeit at the price of less certain redshifts. We will also connect the low-luminosity end of the QLF to

that of Seyfert galaxies measured from the SDSS galaxy sample (Hao et al. 2005b) and explore the continuity of the AGN population at low redshifts and luminosities. We will explore the dependence of the luminosity function on color to determine, for example, whether the luminosity function of intrinsically red quasars (Richards et al. 2003) has the same slope and varies with redshift the same way that blue quasars do; differences could indicate correlations of color with a physical parameter such as accretion rate, mass, or orientation or possible redshift- or luminosity-dependent dust obscuration. Finally, a number of groups are carrying out deeper spectroscopic quasar surveys based on deep SDSS photometry (see Richards et al. 2005; Jiang et al. 2006), and we can look forward to a yet more comprehensive view of the QLF in a few years' time.

APPENDIX

The following query, in SQL, was used to construct the sample of DR3 quasar candidates selected from the TARGET photometry from the SDSS CAS. We note that it is *not* possible to do this query using the public DR3 CAS, as the "region" information that is needed for simultaneously determining the target selection version and area thereof is lacking in that database. However, this information will be available for SDSS Data Release 5.

```
—Query the table that includes all targeted objects
SELECT * FROM Target as t
—Match to the tables with geometry and version information
inner join Region as r on t.regionid = r.regionid
inner join TargetInfo as ti on t.targetid = ti.targetid
—Extract the TARGET photometry
inner join TARGDR3..photoTag as p on ti.target objid = p.objid
—Match to objects with spectroscopy
left outer join specObj as s on s.targetid = t.targetid
```

```
WHERE (
```
—Restrict sample to target selection version v3_1_0
```
        r.regionid in (
                select b.boxid
                from region2box b, tilinggeometry g
                where b.boxtype = 'SECTOR'

                        and b.regiontype = 'TIPRIMARY'
                        and b.id = g.tilinggeometryid

                group by b.boxid
                having min(g.targetversion) ≥ 'v3_1_0'
        ) AND
```
—Include only "primary" objects
```
        ((p.mode = 1) AND ((p.status & 0x10) > 0) AND ((p.status & 0x2000) > 0))
```
—Include only explicit quasar targets
```
        AND ((p.primTarget & 0x0000001f) > 0)
)
```

The restriction on `region` (defined by the intersection of various survey geometric constraints, such as the intersection of an imaging scan and a spectroscopic plate) limits the sample to targets selected with version v3_1_0 and later of the targeting algorithm. The restrictions on `mode` and `status` restrict the sample to the "primary" observations of each object (ignoring any repeat "secondary" observations that exist) that are within the nominal DR3 footprint (some areas with DR3 imaging formally belong to later data releases due to geometric definitions). The bitwise AND restriction on the `primTarget` values returns only quasar candidates selected by the main quasar selection algorithm (Richards et al. 2002).

The joins[27] with `TargetInfo` and `TARGDR3..photoTag` are necessary to extract the TARGET (as opposed to BEST) photometry that will be used in our analysis. The join on `specObj` allows the extraction of spectroscopic parameters from the database.

---

[27] The intersection of two database tables. An inner join returns only objects that exist in both tables. A left outer join returns output for each object in the "left" table, regardless of whether it has a match in the "right" table.

REFERENCES

Abazajian, K., et al. 2003, AJ, 126, 2081
———. 2004, AJ, 128, 502
———. 2005, AJ, 129, 1755
Adelman-McCarthy, J. K., et al. 2006, ApJS, 162, 38
Anderson, S. F., et al. 2003, AJ, 126, 2209
Avni, Y., & Bahcall, J. N. 1980, ApJ, 235, 694
Barger, A. J., Cowie, L. L., Mushotzky, R. F., Yang, Y., Wang, W.-H., Steffen, A. T., & Capak, P. 2005, AJ, 129, 578
Becker, R. H., White, R. L., & Helfand, D. J. 1995, ApJ, 450, 559
Begelman, M. C. 2004, in Coevolution of Black Holes and Galaxies, ed. L. Ho (Cambridge: Cambridge Univ. Press), 375
Blanton, M. R., Lin, H., Lupton, R. H., Maley, F. M., Young, N., Zehavi, I., & Loveday, J. 2003a, AJ, 125, 2276
Blanton, M. R., et al. 2003b, ApJ, 592, 819
Boyle, B. J., Shanks, T., Croom, S. M., Smith, R. J., Miller, L., Loaring, N., & Heymans, C. 2000, MNRAS, 317, 1014
Boyle, B. J., Shanks, T., & Peterson, B. A. 1988, MNRAS, 235, 935
Brown, M. J. I., et al. 2006, ApJ, 638, 88
Chiu, K. 2004, BAAS, 205, 167.04
Collinge, M. J., et al. 2005, AJ, 129, 2542
Cowie, L. L., Barger, A. J., Bautz, M. W., Brandt, W. N., & Garmire, G. P. 2003, ApJ, 584, L57
Croom, S. M., Smith, R. J., Boyle, B. J., Shanks, T., Miller, L., Outram, P. J., & Loaring, N. S. 2004, MNRAS, 349, 1397
Di Matteo, T., Croft, R. A. C., Springel, V., & Hernquist, L. 2003, ApJ, 593, 56
Di Matteo, T., Springel, V., & Hernquist, L. 2005, Nature, 433, 604
Elvis, M., et al. 1994, ApJS, 95, 1
Fabian, A. C. 1999, MNRAS, 308, L39
Fan, X. 1999, AJ, 117, 2528
Fan, X., et al. 2001, AJ, 121, 54
———. 2004, AJ, 128, 515
Ferrarese, L., & Merritt, D. 2000, ApJ, 539, L9
Finlator, K., et al. 2000, AJ, 120, 2615
Fukugita, M., Ichikawa, T., Gunn, J. E., Doi, M., Shimasaku, K., & Schneider, D. P. 1996, AJ, 111, 1748
Gebhardt, K., et al. 2000, ApJ, 539, L13
Goldschmidt, P., Miller, L., La Franca, F., & Cristiani, S. 1992, MNRAS, 256, 65P
Granato, G. L., De Zotti, G., Silva, L., Bressan, A., & Danese, L. 2004, ApJ, 600, 580

Gunn, J. E., et al. 1998, AJ, 116, 3040
———. 2006, AJ, 131, 2332
Haas, M., et al. 2004, A&A, 419, L49
Hao, L., et al. 2005a, AJ, 129, 1795
———. 2005b, AJ, 129, 1783
Hasinger, G., Miyaji, T., & Schmidt, M. 2005, A&A, 441, 417
Heckman, T. M. 1980, A&A, 87, 152
Heckman, T. M., Kauffmann, G., Brinchmann, J., Charlot, S., Tremonti, C., & White, S. D. M. 2004, ApJ, 613, 109
Hewett, P. C., Foltz, C. B., & Chaffee, F. H. 1993, ApJ, 406, L43
Hogg, D. W. 1999, preprint (astro-ph/9905116)
Hogg, D. W., Baldry, I. K., Blanton, M. R., & Eisenstein, D. J. 2002, preprint (astro-ph/0210394)
Hogg, D. W., Finkbeiner, D. P., Schlegel, D. J., & Gunn, J. E. 2001, AJ, 122, 2129
Hopkins, P. F., Hernquist, L., Cox, T. J., Di Matteo, T., Martini, P., Robertson, B., & Springel, V. 2005, ApJ, 630, 705
Hopkins, P. F., et al. 2004, AJ, 128, 1112
———. 2006, ApJS, 163, 1
Hubeny, I., Agol, E., Blaes, O., & Krolik, J. H. 2000, ApJ, 533, 710
Hunt, M. P., Steidel, C. C., Adelberger, K. L., & Shapley, A. E. 2004, ApJ, 605, 625
Ivezić, Ž., et al. 2002, AJ, 124, 2364
———. 2004, Astron. Nachr., 325, 583
Jester, S., et al. 2005, AJ, 130, 873
Jiang, L., & Fan, X. 2006, AJ, submitted
Kennefick, J. D., Djorgovski, S. G., & de Carvalho, R. R. 1995, AJ, 110, 2553
Koo, D. C., & Kron, R. G. 1988, ApJ, 325, 92
Lawrence, A. 1991, MNRAS, 252, 586
Lupton, R. H., Gunn, J. E., Ivezić, Z., Knapp, G. R., Kent, S., & Yasuda, N. 2001, in ASP Conf. Ser. 238, Astronomical Data Analysis Software and Systems X, ed. F. R. Harnden, Jr., F. A. Primini, & H. E. Payne (San Francisco: ASP), 269
Lupton, R. H., Gunn, J. E., & Szalay, A. S. 1999, AJ, 118, 1406
Lupton, R. H., Ivezić, Ž., Gunn, J. E., Knapp, G., Strauss, M. A., & Yasuda, N. 2002, Proc. SPIE, 4836, 350
Marshall, H. L. 1985, ApJ, 299, 109
Meiksin, A. 2005, MNRAS, 356, 596
Merloni, A. 2004, MNRAS, 353, 1035
Oke, J. B., & Gunn, J. E. 1983, ApJ, 266, 713
Oke, J. B., & Sandage, A. 1968, ApJ, 154, 21

Osmer, P. S. 1982, ApJ, 253, 28

Page, M. J., & Carrera, F. J. 2000, MNRAS, 311, 433

Pei, Y. C. 1995, ApJ, 438, 623

Peterson, B. M. 1997, An Introduction to Active Galactic Nuclei (Cambridge: Cambridge Univ. Press)

Pier, J. R., Munn, J. A., Hindsley, R. B., Hennessy, G. S., Kent, S. M., Lupton, R. H., & Ivezić, Ž. 2003, AJ, 125, 1559

Press, W. H., Teukolsky, S. A., Vetterling, W. T., & Flannery, B. P. 1992, Numerical Recipes in C: The Art of Scientific Computing (Cambridge: Cambridge Univ. Press)

Richards, G. T., et al. 2001, AJ, 121, 2308

———. 2002, AJ, 123, 2945

———. 2003, AJ, 126, 1131

———. 2004a, ApJS, 155, 257

———. 2004b, AJ, 127, 1305

———. 2005, MNRAS, 360, 839

———. 2006, AJ, 131, 49

Scannapieco, E., & Oh, S. P. 2004, ApJ, 608, 62

Schlegel, D. J., Finkbeiner, D. P., & Davis, M. 1998, ApJ, 500, 525

Schmidt, M. 1963, Nature, 197, 1040

———. 1968, ApJ, 151, 393

Schmidt, M., & Green, R. F. 1983, ApJ, 269, 352

Schmidt, M., Schneider, D. P., & Gunn, J. E. 1995, AJ, 110, 68

Schneider, D. P., et al. 2003, AJ, 126, 2579

———. 2005, AJ, 130, 367 (DR3Q)

Schneider, P., Ehlers, J., & Falco, E. E. 1992, Gravitational Lenses (Berlin: Springer)

Scott, J. E., Kriss, G. A., Brotherton, M., Green, R. F., Hutchings, J., Shull, J. M., & Zheng, W. 2004, ApJ, 615, 135

Scranton, R., et al. 2002, ApJ, 579, 48

Seyfert, C. K. 1943, ApJ, 97, 28

Silk, J., & Rees, M. J. 1998, A&A, 331, L1

Smith, J. A., et al. 2002, AJ, 123, 2121

Spergel, D. N., et al. 2003, ApJS, 148, 175

Stoughton, C., et al. 2002, AJ, 123, 485

Strateva, I. V., Brandt, W. N., Schneider, D. P., Vanden Berk, D. G., & Vignali, C. 2005, AJ, 130, 387

Tananbaum, H., et al. 1979, ApJ, 234, L9

Telfer, R. C., Zheng, W., Kriss, G. A., & Davidsen, A. F. 2002, ApJ, 565, 773

Treister, E., & Urry, C. M. 2005, ApJ, 630, 115

Treister, E., et al. 2004, ApJ, 616, 123

Tremaine, S., et al. 2002, ApJ, 574, 740

Tucker, D., et al. 2005, AJ, submitted

Ueda, Y., Akiyama, M., Ohta, K., & Miyaji, T. 2003, ApJ, 598, 886

Vanden Berk, D. E., et al. 2001, AJ, 122, 549

———. 2005, AJ, 129, 2047

Wall, J. V., Jackson, C. A., Shaver, P. A., Hook, I. M., & Kellermann, K. I. 2005, A&A, 434, 133

Wampler, E. J., & Ponz, D. 1985, ApJ, 298, 448

Warren, S. J., Hewett, P. C., & Osmer, P. S. 1994, ApJ, 421, 412

Weinstein, M. A., et al. 2004, ApJS, 155, 243

Wisotzki, L. 2000, A&A, 353, 861

Wisotzki, L., Christlieb, N., Bade, N., Beckmann, V., Köhler, T., Vanelle, C., & Reimers, D. 2000, A&A, 358, 77

Wolf, C., Wisotzki, L., Borch, A., Dye, S., Kleinheinrich, M., & Meisenheimer, K. 2003, A&A, 408, 499

Wyithe, J. S. B., & Loeb, A. 2003, ApJ, 595, 614

York, D. G., et al. 2000, AJ, 120, 1579

Yu, Q., & Tremaine, S. 2002, MNRAS, 335, 965

Zakamska, N. L., et al. 2003, AJ, 126, 2125